2014-11-21

An Optical Tracking System for Radiosurgery of Uveal Melanoma by CyberKnife

Hairong Chen
University of Miami, h.chen19@umiami.edu

UNIVERSITY OF MIAMI

AN OPTICAL TRACKING SYSTEM FOR RADIOSURGERY OF UVEAL MELANOMA BY CYBERKNIFE

By

Hairong Chen

A DISSERTATION

Submitted to the Faculty

of the University of Miami

in partial fulfillment of the requirements for

the degree of Doctor of Philosophy

Coral Gables, Florida

December 2014

UNIVERSITY OF MIAMI

AN OPTICAL TRACKING SYSTEM FOR RADIOSURGERY OF UVEAL MELANOMA BY CYBERKNIFE

Hairong Chen

A dissertation submitted in partial fulfillment of
the requirements for the degree of
Doctor of Philosophy

Approved:

_____
Weizhao Zhao, Ph.D.
Professor of
Biomedical Engineering

_____
Xiaodong Wu, Ph.D.
CEO
Biophysics Institute of America
Miami, Florida

_____
Fabrice Manns, Ph.D.
Professor of
Biomedical Engineering

_____
Jorge Bohorquez, Ph.D.
Associate Professor of
Biomedical Engineering

_____
Edward A.Dauer, M.D.
Research Associate Professor of
Biomedical Engineering

_____
M. Brian Blake, Ph.D.
Dean of the Graduate School

_____
Yidong Yang, Ph.D.
Assistant Professor of
Radiation Oncology

CHEN, HAIRONG (Ph.D., Biomedical Engineering)
An Optical Tracking System for Radiosurgery of Uveal Melanoma by CyberKnife (December 2014)

Abstract of a dissertation at the University of Miami.

Dissertation supervised by Professor Weizhao Zhao.
No. of pages in text. (114)

Uveal melanoma is the most common primary intraocular tumor in adults. One of the effective managements of ocular melanoma is the localized radiation treatment. In addition to the commonly performed invasive radioactive plaque brachytherapy, using focused external photon radiations, x-rays or gamma rays, have emerged as treatment options. However, these radiation delivery methods are either involved with the invasive surgical operation or limited by the gantry movement to account for the involuntary movement of the eyeball. The goal of this doctoral research is to design and validate a method that can offer a non-invasive radiosurgery for uveal melanoma and to compensate for the eyeball's movement. The Cyberknife system, driven by a robotic arm with 6D freedom of motion and guided by the x-ray stereotactic and infrared cameras, was chosen as the radiosurgery platform to investigate the feasibility of the method designed in this research.

The essence of this study demonstrates the non-invasive tumor tracking capability through the data transformation by tracking the pupil in real time. The research was conducted in three stages. We first performed a computer graphical simulation, in which the eyeball, the intraocular tumor, and the pupil were all simulated by mathematical models. We successfully proved that the pupil's 2D projection on the image plane

(captured by a camera) relates to the tumor's 3D location. We derived a 2D/3D transformation, a linear model linking the pupil's 2D coordinate and the tumor's 3D coordinate. This model laid a mathematical foundation for the research. The error prediction analysis was also performed in the simulation. In the second stage of the research, we built a mechanical phantom, which is a prototype to implement the designed method. The mechanical phantom consists of a camera module, an eyeball module, an eyeball holder module, and an eyeball motion module. In the third stage of the research, we performed the validation by using the mechanical phantom under the CT and CyberKnife machines. Under the CT machine, the captured pupil's positions were associated with the scanned tumor's positions so that we generated the 2D/3D transformation. We then moved the mechanical phantom under the Cyberknife system. After the re-alignment of the phantom, we used the newly tracked pupil position to predict the tumor position. Based on the promising outcomes, we concluded that the designed non-invasive pupil tracking method for the tumor tracking under the Cyberknife system is a feasible approach and is ready for the dosimetry validation.

This dissertation presents, in details, the above mentioned research stages and includes an introduction of the physiology and anatomy of the eye and uveal melanoma (Chapter 1), a review of radiosurgery methods (Chapter 2), descriptions of the optical tracking mechanism and the derivation of the 2D/3D transformation (Chapter 3), descriptions of the mechanical phantom (Chapter 4) and system integration (Chapter 5), discussion and conclusion of the research (Chapter 6 and 7).

Acknowledgment

It has been an invaluable experience for me to work with Dr. Zhao, my advisor. He shows his outstanding academic guidance throughout my research. He can always bring good advices and ideas, and enlighten me to move forward when I encounter obstacles. He gives me treasurable suggestions for career development in the future.

I also extend my gratitude to Dr. Wu. He guides me academically, shares his priceless ideas from his accomplished clinical experience, and puts his efforts to conduct our experiments. Sincerely thanks to Dr. Manns, Dr. Bohorquez, Dr. Dauer, and Dr. Yang, the committee members, for their brilliant suggestions and comments to this dissertation.

Special thanks to Mr. Richado Garcia and Mr. Alejandro Gonzalez for devoting their time and efforts in the design and development of the mechanical hardware. Sincere thanks to Dr. Georges F. Hatoum for offering experiment facilities. I also appreciated to Mr. Alehandro Iglesias for his assistance in CT simulation. This research was sponsored by NSF grand DUE 1022750.

Finally, I would like to extend my deepest gratitude to my fellow colleagues, my genuine friends, and my perseverant parents for their supports, encouragements, and understanding.

TABLE OF CONTENTS

Page

LIST OF FIGURES

LIST OF TABLES

Chapter 1 Introduction

1.1 Physiology of Eyes

The eyes are essential for human beings to see the colorful world. The basic physiological knowledge of the eye is helpful not only for better understanding how it works, but also paving the way to investigate causes and treatment options for eye diseases.

The eye [1] is an organ specialized for the detection, localization, and the analysis of light by definition. The eyeball can be separated into three chambers from the sagittal plane: the anterior chamber, the posterior and the vitreous chamber. The anterior and posterior chambers are both fluid-filled (aqueous humor) and separated by the iris. The boundary for the anterior chamber is from the cornea to the iris, and the iris to the lens for the posterior chamber. It is the posterior chamber that enables the accommodation for distance vision. The vitreous chamber has the largest volume, filled with amorphous and gelatinous material different from the fluid filled in the other two chambers. From another point of view, the eyeball is an enclosed capsule, consisting of fiber cells and covered with a layer of anterior epithelium without blood supply. It is wrapped by three layers: the outer, the inner, and the middle layer. The outer layer is the sclera or white of the eye, giving a spherical shape of the eye for the posterior chamber, and the cornea for the anterior chamber. The inner layer in the vitreous chamber is named retina, consisting of the neural sensor to transfer light energy into neural signal. The middle layer is called choroid, which is rich of blood vessels; it is between the outer and the inner layer.

Each specific structure in the eye plays its unique physiological role and will reflect corresponding symptoms when it comes to eye diseases. For instance, the cornea is

transparent to allow the light getting into the deeper parts. Behind the cornea, the iris gives the color of an eye and serves like a window to change the size of the incident light beams to control the light level on the retina. It is the suspended ligaments attached to the ciliary muscles that alter the shape of the lens to perform accommodation. If there is clouding happening to the lens, especially for older adults or patients, it is called cataract. It could be a side effect of one type of radiation as well, which will be introduced in the later chapter. Behind the lens, light is supposed to pass through the vitreous body before reaching the retina. As the intraocular pressure increases, the vitreous chamber transfers the pressure to the entire eye, leads to the compressing and damaging of the weak point at the outlet of the optic nerve, and ultimately impairs the vision gradually. This type of eye disorder is named glaucoma, which also could be an irradiation-related complication. In terms of layers of the eyeball, the choroidal layer provides blood, oxygen and nourishment to the retina. At the same time, it is the most popular growing house for ocular tumor, and in fact, choroidal melanoma is very typical, and will be discussed in the uveal melanoma section.

Some types of visual assessment are recommended here to show the physiological performance for the normal eyes or those after treatments. For instance, visual acuity is the ability of the eye to distinguish two nearby points, and especially depends on the spacing of photoreceptors in the retina and the precision of an eye's refraction. The distance across the retina can be expressed in terms of degrees of the visual angle.

From the perspective of eyeball movements, several muscles are responsible for the dynamic movement, which are attached to the eyeball. They are the medial rectus, lateral rectus, inferior rectus, superior rectus, inferior oblique and the superior oblique. The

medial and the lateral rectus serve the primary abduction of the eyeball; the inferior and the superior rectus accomplish depression and elevation movement; and the inferior and the superior oblique offer excycloduction and incycloduction. Here, the abduction is the movement of the eye rotating around the vertical axis that moving nasalwardly or templewardly. The rotations around the horizontal axis refer to the elevation and depression that moving upwardly or downwardly. The abductions along the four directions (upward, downward, nasalward and templeward) are the primary movement. Excycloduction and incycloduction movement are the combination of rotations around the vertical axis and the horizontal axis.

It raises a question: since the eyeball muscles can drive the eyeball into different directions, why is the picture that people are seeing every second horizontally paralleled to the eyeball? In general, there are three degrees of freedom involved in eyeball rotation. However, when the head is fixed, the degrees for gazing drop to two, by giving up the rotation around the anterior-posterior, i.e. the light beam path. According to the Donders' law, the rotation around the anterior-posterior axis is severely restricted [2], serving as one of the fundamental ocular motility. Listing and Helmholtz [2] especially suggested that each eye movement from the primary position to any other position involves a rotation around a single axis lying in the equatorial plane, or Listing's plane, where the vertical and horizontal axes sit in. On the other hand, if unrestricted rotations around the line of the incident light occur, the cardinal rotations and their combinations could be associated with an infinite number of cyclorotations. This will result in great difficulties in spatial orientation.

The compensation can be found from the contradiction between the eyeball muscles. For example, the contract of the inferior rectus not only makes the eye look down, but also brings a slight rotation along the anterior-posterior axis, which means the top of the eye moves medially. However, it is the contradictory oblique superior and the inferior rectus that correct the undesirable movement of the eyeball conjunction with the inferior rectus to ensure the eye moves downward. Similar scenario happens to the superior rectus to keep the vision view horizontally paralleled.

As a prerequisite knowledge of our phantom system, it is necessary to get familiar with the eyeball dimensions as references. In human beings, the eyeball is close to a sphere and the averaged diameter is around 26mm; the thickness of cornea is proximately 0.5mm, the anterior-posterior length of lens is about 3.2mm, and the distance between the posterior cornea to the anterior surface of lens is around 2.8mm. The diameter of the pupil is 3 to 5mm and dilates under a dark light environment. At the same time, the center of the pupil will shift according to the original center when the accommodation happens. Studies [88] show that the mean magnitude of the pupil shift was 0.084 +/- 0.069mm from mesopic to photopic, 0.149 +/- 0.08mm from photopic to pharmacologic dilation, and 0.102 +/- 0.104 mm from mesopic to pharmacologic dilation. This phenomenon requires further consideration while evaluating the performance of our research and the setup of the light level in the radiosurgery room.

In summary, the eye works through the combination of different structures in the organ. The failure of each of them, such as the lens, the choroid, or the uvea, could bring up certain diseases. The related symptoms could serve as evaluations for the outcome of treatment.

1.2 Uveal Melanoma

Epidemiologically, uveal melanoma [3-11] is the most common primary intraocular malignancy in adults. It dominates the ocular melanoma by around 85%. There are 7 new cases per million per year in most western developed countries, approximately 1,200 to 1,400 new melanomas happen annually. No change has been reported in the incidence of uveal melanoma over the past 30 years in USA and some European countries, such as Finland or Denmark. However, the incidence of uveal melanoma in Sweden from 1960 to 1998 indicates a relatively annual decrease by 1%. From the racial point of view, uveal melanoma occurs in a lower rate in the black and the Asian population compared with a higher rate in USA, European countries, Australia and New Zealand populations. In terms of the age factor, it is found that the incidence rate increases with age, especially around 70 years.

Pathologically, uveal melanoma occurs along the uveal track from the iris, the ciliary to the choroid layer. They are named as iris melanoma, ciliary melanoma and choroidal melanoma [4]. Most of them occur at the posterior chamber, because the choroidal layer is rich of blood vessels to bring nourishment for both the normal tissue and the tumor. The choroidal melanoma extends from the vascular layer and pushes the inner layer into the vitreous humor. Around 75 percent of such tumors appear in a “dome” shape. The rest of them erode through the so-called Bruch’s membrane and result in a “collar-bottom” or “mushroom” shape [13]. In terms of the type of ocular tumor in the choroidal layer, the diffuse choroidal melanoma is an aggressive rare case; and the small choroidal melanoma is usually tagged with superficial orange pigment. As a result, the vision gets worse due to the extension force and lesions. The extended large tumor into the retina will result in

the detachment and jeopardize the visual field and vision. The large peripheral lesion and hemorrhage decrease the visual acuity eventually. Regarding the iris malignant tumors, most of them are benign and do not need intervention treatment, because they are easily diagnosed due to the abnormal pigment or the distortion of the pupil. With respect to the ciliary melanoma, it could reach a larger size due to its asymptomatic characteristic. It brings a "sentinel" episcleral vessel, a distortion of the lens and results in an uncorrectable astigmatism. The high pressure extending toward the lens from the ciliary body ends up with local dense cataract. A ring melanoma is a rare case for ciliary melanoma [11,12,13].

The origin of uveal melanoma could be primary or metastasis. The primary ocular tumor dominates in the occurrence of ocular tumors. There are only 1% to 4% of patients diagnosed as the primary melanoma announced system metastases. There is a low metastatic incidence happening to the special vascular structure in the uveal track, because there are no lymphatic channels to spread the tumor cells. The metastases to the eye is rare, but it is common for uveal melanomas to be transferred to the liver by approximately around 90 percent, and the rest from the lungs and the bones. With the knowledge of metastasis from the primary uveal melanoma, it is helpful for the treatment planning and the execution of radiotherapy and/or radiosurgery [11, 14, 19]. The progression of uveal melanoma is related to the early stage of oncogenic mutations, which have an impact on the pathways to control the cell cycle or cell apoptosis [3]. For skin melanoma, many epidemiological causative factors could be obtained, including the hair color, and the sun light exposure, etc[4-10]. However, in the case of uveal melanomas, it is hard to find the correlated epidemiological factors.

Another risk factor for uveal melanoma is the size, which is related to the survival rate and essential for the treatment options. There are two parameters describing the size of a uveal melanoma: thickness and basal diameter. The basal diameter is the largest diameter of the tumor, and the thickness is the height perpendicular to the basal plane. Studies[15-17] show that there is a relationship between the size of tumor and the actuarial survival curves, demonstrating that the lower survival rate is corresponding to the larger tumor. These dimensions also contribute to the calculation of the tumor volume, which is associated with the decision of treatment and the consecutive treatment planning. Traditionally, the uveal melanomas are divided into three categories: large, medium and small size. According to the standard from the Collaborative Ocular Melanoma Study (COMS) [16], the large tumor has the thickness more than 8 mm and/or the basal diameter greater than 16 mm; the medium size tumor has the thickness, range 3.1 mm to 8 mm and the basal diameter no more than 16 mm; and the small size tumor embraces the thickness from 1 to 3 mm and the basal diameter is as least 5mm. Other studies [11] propose different criteria for three categories, such as taking thickness of 10 mm and the basal diameter of 16 mm to distinguish the large size and the medium size, 2.5 mm in the thickness and 10 in the basal diameter for the medium and the small size tumor. A much more detailed classification [15] is addressed by the American Joint Committee on Cancer Classification of Posterior Uveal Melanoma in 7731 Patients, which advocates 4 categories with the combination of the thickness and the basal diameter. The criteria are more comprehensive, because of including the extreme conditions into categories. For example, tumor with the thickness less than 3 mm and the basal diameter greater than

18mm or a size of thickness greater than 15 mm and a basal diameter less than 3 mm, falls into category 4, which does not appear in other classifications.

The cell type of uveal melanoma plays a fundamental role to predict the survival rate after therapy. It is similar to the role of the cytologic classification for cutaneous melanomas. It can be categorized as a benign or malignant spindle cell, or epithelioid cells mixed with certain amount of spindle cells and necrotic cells [17, 19, 20]. A mixture of the above cells is observed for majority of uveal melanomas. Studies show that the patient survival rates of uveal melanoma of the spindle cell type was approximately twice of those with the mixed cell types.

In sum, the uveal melanoma is a rare disease, but has the potential to be developed into malignant tumors. The location, the classification, the origin, the size, the symptoms and other physical features, are risk factors needed to be considered for the diagnosis, the treatment, and the follow-up studies.

1.3 Treatment Options

Effective treatment options available to combat uveal melanomas include the surgical resection, the hyperthermia therapy, the radiotherapy and some combined ways. Studies and clinical experiences indicate that different treatments are chosen for different occasions. For the iris melanomas, observation with careful follow-up, the local resection, enucleation, and the plaque radiation are the choices. For ciliary body melanomas, the plaque brachytherapy [25-26], the external-beams, local tumor resection, and enucleation are the better options. For the small choroidal melanomas mentioned above, more options are available: observation, plaque radiation therapy, external-beam, Gamma Knife radiosurgery, transpupillary thermotherapy, local tumor resection and enucleation. For

the medium and large choroidal melanomas, the options are: plaque brachytherapy, external beam, local eye-wall resection, combined therapy, and enucleation.

Surgical treatments of ocular tumors can be particularly traced back to the early twentieth century, including the whole eyeball enucleation and the partial resection for posterior choroidal melanomas. Enucleation [2, 4, 16, 17, 18, 21, 22] becomes a primary treatment under the following conditions: the progressive tumors occupy most of the intraocular space, the affected eyes have a severe secondary glaucoma, the diseased eye almost does not retain any function after an alternative treatment or failed that treatment, or a significant ocular neovascularization shows up before the surgery and especially with the request of patients after notifying the situation. The residual tumor cells are recognized for 6% cases and the local recurrences due to surgery were found by microscopic examination. It shows the potential risk for surgery resection. Because the incomplete resection is a common concern for the choroidal melanoma, under the situation that no knowledge of the exact boundary of the tumor is definitive, and that the metastases might evolve to other organs after the surgery.

So far, in addition to the traditional surgery resection of uveal melanomas, the radiation and combined treatments become the main flow and be unfolded in the next chapter in detail.

1.4 Problem Statement and Motivation

Literatures cast attainable options to treat the most common primary ocular tumor happening in adults. Originally enucleation intending to remove the diseased eyeball serves as a primary treatment for the large sized ocular tumor before the application of radiation in the field of ophthalmology. In this way, patients are required to undergo

clinical operation and exposed to a higher chance for tumor metastasis. In light of the advance of radiological physics since the 1900s, the radiosurgery and radiological treatment become a feasible choice for the treatment of uveal melanoma. For instance, the plaque brachytherapy utilizes the radioactive gamma rays or beta rays emitting from isotope sources attached to the tumor region. It cannot skip the surgery procedure to implant the plaque. The Gamma Knife can obtain high precision by virtue of the distribution of gamma ray source around a hemisphere, but patients have to experience the painful procedure to have the rigid helmet collimator attached to the skull. As the proton therapy is concerned, it holds the advantage of depositing energy at a precise location so as to reduce the ionization for the surrounding normal tissues. Meanwhile, this type of high accuracy machine demands the fiducial markers attaching around the sclera, so the surgical operation is unavoidable. The most prevalent option is the stereotactic radiosurgery based on the LINAC, which deliver photon or electron beams for treatment. However, the design of the gantry for such series of machines is limited to the rotation around an isocenter, even if the couch movement comes as the compensation to reach the beam delivery angle. Fortunately, this limitation is conquered by the CyberKnife machine, which can attain higher degree of movement by adopting a robotic arm. In addition, this machine incorporates another advantage, the so-called image guidance radiotherapy (IGRT) to point out the tumor location in real time.

In the case of radiotherapy for ocular tumors, it involves irregular eyeball movements: voluntary and unpredictable involuntary movements, such as saccades. There are two ways to deal with this occasion. One of them goes to the regional anesthesia to freeze the eyeball during treatment with the cost of uncomfortableness and the reproducibility

issues between the treatment planning and the therapy stages. Another way follows the gating or the 4D technology to supervise the regular movement of the chest wall or abdomen by reference to the patient's EEG or breathing model. However, the eyeball movement has no regular rhythm to follow. Applying the radiation treatment for ocular tumors without the participant of anesthesia becomes a challenge due to the irregular eyeball movement.

As a solution, our motivation focuses on addressing an idea to fulfill a noninvasive radiosurgery for ocular tumor by CyberKnife. It will borrow the noninvasive concept from the patient's standing point, has more degree of freedom for beam delivery by adopting the CyberkNife machine, and most importantly proposes an approach for eyeball tracking. In this study, we need to have an essential 2D/3D transformation algorithm to predict the tumor location in real time, and to developed a feasible noninvasive phantom system to testify the transformation algorithm and completed two types of validation to evaluate the systematic quality. Further irradiation validation will be performed as the fore step for the clinical trials and treatments.

This dissertation is composed by the following chapters. Chapter 2 gives the fundamental background knowledge with respect to radiation and radiosurgery. Chapter 3 focuses on the workflow of the system and the derivation of the 2D/3D transformation algorithm. Chapter 4 brings specific pictures of each component of the mechanical phantom system. Chapter 5 concentrates on the system integration and system performance. In the end, Chapter 6 conveys the discussion part, and Chapter 7 takes care of the conclusion of this dissertation.

Chapter 2 Review of Radiation Treatment

2.1 Background of Radiation Physics

Radiation physics is the fundamental principle behind the technology of radiation treatment. It is the science of the ionizing radiation, its interaction with the matter, and especially the absorbed energy. The radiation physics started from the discoveries of the x-rays by Whilhelm Rontgen, the radioactivity by Henri Beccquerel, and the radium by the Curies in the 1890s. Within a very short period time both x-rays and radium became useful tools in the medical field. The first x-ray photograph (of Mrs. Rontgen's hand) was taken by Rontgen late in 1895, and coincidently the radioactivity was discovered by Henri Beccquerel in 1896.

Radiation physics focuses on ionizing radiation, which investigates the interaction between the matter and the energized beams, and is generally characterized by the ability to excite and ionize the atoms of matter it interacts with. The termed "ionizing" means radiations need to carry the kinetic or quantum energy beyond the valence energy holding the electrons from escaping from an atom. The ionizing radiations can liberate from the γ-rays, x-rays, fast elections, heavy charged particles and the neutrons beams. The Gamma –rays (γ-rays) are electromagnetic radiation collected from a nucleus or in annihilation reactions between the matter and the antimatter. The X-rays refer to a radiation emitted by charged particles (usually electrons) in changing atomic energy levels (characteristic or fluorescence x-rays) or in slowing down in a Columb force field (continuous or bremsstrahlung x-rays). In terms of the fast electrons, they are called β-rays (positive or negative) emitted from a nucleus. The energy could also refer to δ-rays as the outcome of a charged-particle collision. The heavy particles include proton,

deuteron, triton, alpha particle, pions and other heavy charged particles consisting of nuclei of the heavier atoms. They can be obtained from the acceleration by a Coulomb force field in a Van de Graaff, cyclotron, or heavy-particle linear accelerator. In particular, alpha particles can be gathered from certain radioactive nuclei as well. Neutral particles are emitted from nuclear reactions, and cannot get acceleration in an electrostatic way.

The radiation ionization can be classified into directly ionizing and indirectly ionizing. The directly ionizing radiation usually indicates fast charged particles, which deliver their energy to the matter straightforwardly by means of amount of small Coulomb-force interactions along the particle's track. Indirectly ionizing refers to the X-rays or γ-rays or neutrons, which evolves a second step process after transferring their energy to the charged particles in the matter. The indirect ionization dominates by two thirds of the whole ionizing radiation. Biologically, the highly concentrated absorbed energy from ionization can lead to the cytologic apoptosis directly or through the indirect function of free radicals, which are atoms or compounds with an unpaired electron accompanied with high reactivity and chemically toxicity in water medium.

Under clinical circumstances, there are two sources of radiation beams: isotopes and linear accelerators. The Gamma rays, alpha rays and beta rays are the outcome of the isotopic decays. The Gamma ray engages a higher energy and can be blocked by thick metal (lead). The Alpha ray has the lowest energy and can be stopped by a piece of paper. The energy level of the beta ray stays in between the alpha and the gamma rays, which can be absorbed by a thin metal layer (gold, lead). The radiation generated from the linear accelerator could be the photon beams, the electron beams and the charged particle beams (alpha particle, proton). The radiation production process starts from the injection of the

low energy electrons from an electron gun at one end of the accelerating waveguide, which is responsible for accelerating electrons linearly to high velocity, approaching the light speed. Then the high energy electrons are redirected toward the center of the beam's gantry by a magnetic bending assembly. If photon beam is selected for radiotherapy, the high energy electron beams will hit on a metal target (tungsten) to kick out the bremsstrahlung emission. If electron beam is chosen, an electron applicator will be employed.

In summary, radiation physics plays an essential rule as the guidance offering the knowledge of the radiation ionization, the interaction between matters, the ways to obtain different types of energy beams, and the potentially application according to their characteristics.

2.2 Background of Radiobiology

The radiobiology deals with the effect and impacts of ionizing radiation in the living body. With the knowledge of the radiation physics, the radiation source could be charged or uncharged high energy beams with different mechanisms in energy transferring. In the case of the x-rays and the γ-rays, they deliver energy to the matter through a photoelectric phenomenon and a Compton scattering. Regarding the neutrons, they interact with the nuclei of atoms of the medium and set in motion as the fast recoil protons, the alpha particles and the heavier nuclear fragments, distinguished by high penetration compared with the charged particles of the same mass and energy.

From the molecular level, the process of ionizing can cause deletions, substitutions, and/or the actual breaks in the DNA chain. If DNA strand brakes cannot get repaired correctly in time, it will lead to the abnormalities in chromosomes to jeopardize the

reproduction integrity. If cells eventually get killed, the biological effect might appear hours to days later when the damaged cells attempt to divide. The oncogenic damage takes a longer time, around 40 years later, to witness the abnormalities in expression. Regarding the mutation damage, it will be delayed by many generations to show up, since it starts from a germ cell to the hereditary changes.

To investigate the risk factors of ionizing radiation, the relative biologic effectiveness indicates the impact of ionizing in tumors and normal tissues. It is defined as the ratio of D_{250}/D_r, where they are the doses of the x-rays and the test radiation required for an equivalent biological effect. There are several contributive factors to the affected biological subject, such as the type of radiation, the radiation dose, the fractionated dose, the dose rate, and the cell types.

Fractionation is an important factor. When the dose is split into two fractions separated by a time interval, more cells will survive than for the time total dose given in a single fraction. As the time interval between the two dose fractions increases, there is a rapid increase in the fraction of cells surviving owing to the prompt repair of the sublethal damage and no incremental benefit for further increase in time. As an effect, the amount of the sublethal damage repair in a split dose varies with the type of radiation. For example, the x-rays with equal fractions and 1 to 4 hours separation, result in a remarkable increase in survival due to the repair of the sublethal damage. This serves as a strong advantage for the radiosurgery with fractionated dose delivery. But when it comes to the neutrons, little effect can be observed with less repair of sublethal damage. In terms of the dose rate, the lower the dose rate combined with longer exposure time window, the reduced radiation effects appear for a certain dose. On the other hand, the higher dose

rate imposes greater influences on the tumor and the adjacent normal tissues. Regarding the intraocular radiotherapy, both the fractionated radiation dose and the dose rate are crucial to reach a balanced outcome.

The radiation technology becomes an effective and efficient alternative to deal with ocular tumors instead of the surgery resection or the enucleation, but at the cost of concerned side effects or complications to the surrounding normal tissues [34-36, 38]. The symptom includes acute erythema, depigmentation, atrophy, telangiectasias, hair loss and ectropion or entropion of the eyelid in general. Different structures will show different symptoms after the irradiation. The radiation related dry eye is due to the malfunction of the lacrimal glands. The natural lens is particularly sensitive to radiation. The radiation induced cataracts progresses via the migration of the abnormal fibers at the posterior pole, due to the injured dividing cells. Since the cell division continues and there is no mechanism to remove the impaired cells, the granular opacities and vacuoles grow into several millimeter in size with clear centers, accumulating at the posterior in the early stage, then migrating back to the anterior part. Regarding the cornea, it is a type of radiation resistant tissue. But the relatively higher dose will lead to the acute corneal toxicity, due to the loss of the epithelium. The sclera can tolerate a relatively higher dose, and few radiation impacts have been recorded. In the case of the iris, the radiation tolerance is a single dose of 10-20 Gy; the complications include the neovascularization and the neovascular glaucoma. In terms of the rest structures, the side effects to the retina, the choroid and the optic nerve are critical to preserve the vision. The radiation retinopathy in the macula imposes a high probability for the vision loss and blindness. It could result in the closure of blood vessels within the optic nerve. Young patients should

be taken more care, because the hypothalamic and the pituitary dysfunction mostly happen to children for radiation to the optic nerve region.

As a conclusion, the radiation to the target tumor and the normal tissue can be evaluated by the term of relative biological effect. The radiation dose, fractionation and dose rate all contribute to the eventual biological effects and should be taken into account for treatment. Particularly, the complications happening to the different structures in the eyeball are listed and should be considered during the treatment planning or re-planning.

2.3 Radiation Treatment

By taking the advantage of radiation physics and considerations of the radiobiological effects, radiation treatment becomes an effective alternative way for cancer treatment. It diverges according to the energy type, the mechanism of beam delivery, and the dose level, etc. For instance, there are the proton therapy, heavy particle treatment, gamma knife, photon beam, and the electron beam radiotherapy with respect to the energy type. There are high and low dose rate brachytherapy according to the delivered dose rate. There is stereotactic treatment compared with brachytherapy in terms of the mechanism of beam delivery. Stereotactic treatment includes stereotactic radiosurgery (SRS) and stereotactic radiotherapy (SRT).

SRS delivers relatively high dose at once or few fractionated doses over a short time (hours, days or weeks) between fractions. In comparison, SRT works with a lower dose and the irradiation is split into a number of fractions over several days or weeks. The dose delivery depends on different modalities, such as the LINAC based x-ray or electron machine, the Gamma Knife, the CyberKnife or proton beam facilities. They produce and

irradiate energy beams to the targets in a stereotactic way so that the beam can be repositioned according to the planning.

The general workflow of the radiation treatment is deployed through the simulation imaging collection, the treatment planning and eventually arrives to the treatment stage. First, the simulation is designed to pick up the comprehensive anatomic information, and transfer the exact autonomic and functional information into the planning stage to bring out a feasible solution, and pull out the whole plan into the ultimate treatment stage. Modern imaging technologies, such as CT, MRI, PET, 4D-CT, PET-CT, are helpful candidates for the simulation. In special, the immobilization of patients is crucial due to the requirement to reproduce the patient's position during planning and the treatment stages. Second, the radiation treatment planning utilizes both the simulation output and the prescription objectives from the oncologist to generate a reasonable and reliable dose distribution upon the region of interest. The treatment planning includes every single component in the treatment modality system, such as the accuracy, precision, dose rate, multileaf collimator, wedges, and bolus in the case of LINAC based stereotactic radiotherapy. Eventually, when the planning obtained the approval from the oncologist and passed the validation from the clinical physicist, the actual radiation will start after the final validation of the planned fields, the beam aperture, etc.

In terms of the treatment of uveal melanoma, there are several options, such as the brachytherapy, Gamma-Knife, LINAC SRT/SRS, CyberKnife, proton therapy and tanspupillary thermotherapy (TTT). Here the TTT is not exact a radiation way but one form of hyperthermia. Each of them will be unfolded in the following sections.

2.4 Plaque Brachytherapy of Uveal Melanoma

The brachytherapy or endocurietherapy, has a long history in clinical application. It was first put forth by Alexander Graham Bell in 1901. This technique is to implant the radioactive source directly into a tumor in variety of forms (needles, tubes, seeds, wires, pellets) so as to preserve the affected eyeball and recover the vision in response to the treatment of uveal melanomas. Usually the seeds are sealed and doubly encapsulated to adequately shield the alpha and beta radiation and also to prevent the leakage from the source. A comprehensive brachytherapy requires taking a series of factors into account, such as the type of radioactive seeds according to radiation physics, the surgical operation to implant the disk and wires, the anatomic information from simulation, and the treatment planning, etc.

There are different types of radioactive sources, such as the Co-60, Cs-137, Ir-192, I-125, Pd-103, Au-198, and Y-90. Here, the Co-60 leads in average photon energy with 1.25 MeV, the Au-198 has the shortest half-life time with 2.7 day, and the Pd-103 has the shortest half value length in lead with 0.01 mm. The Cesium-137 is available in the forms of needles, tubes and pellets. The Iridium-192 is used in the form of wires, seeds and strands of nylon ribbon. The Iodine-125, palladium-103 and gold-198 only appear in the form of seeds and usually are inserted into the tumor volume by an afterload machine.

In the case of the uveal melanoma, the plaque is a common carrier for radioactive seeds. It is usually patched to the sclera surrounding the tumor. The diameter comprises an additional 2mm tumor-free margin for ophthalmoscopy or ultrasonography. The selection of the metallic plaque and how to arrange the seeds depends on the type of the isotope. An additional eye patch, made of lead, may also be used to cover the eye for

shielding. The procedure is performed by the ophthalmologist under a general or local anesthesia. The extraocular muscle will be detached to fix the plaque if it is overlying the tumor. The patients under the plaque brachytherapy can stay in hospital or be outpatient.

In the history of the eye plaque treatment, Moore [23] is the pioneer, who treated the choroidal sarcoma with the radon seeds in 1929. Under a general anesthesia, the radon seeds were inserted into the thickest part of the growth in separated time. The sclerotic incision and bleeding were unavoidable during surgery. As a result, the tumor got shrunk and the vision was preserved. This suggested that 5 millicuries could be used and greater strength is preferable. Stallard adopted the cobalt-60 as sources and implanted the radioactive seeds into the tumor in 1960s. Other types of isotopes were attempted for the treatment of intra-ocular melanoma. Brachytherapy of uveal melanoma became a common alternative to enucleation until 1970s.

Vast investigations have been done for the treatment of ocular tumors with respect to the irradiation source, the blocker and other factors. Regarding eye plaque isotopes [23-31,37, 39], the Cobalt-60 plaques were the most common treatment for uveal melanoma. However, the low-energy sources (I-125, Ru-106/Rh-106, Pa-103) became prospective alternatives by considering radiation safety, because they have a rapid dose fall-off, indicating a high dose gradient to concentrate the dose into the tumor volume so as to reduce complications. Regarding the choice of the blocker for safety concern, to block approximate 50% of the gamma rays emitted from Co-60 plaque requires around 10 mm aluminum, while 1 mm gold can stop 99.95% of low energy emitted from I-125 or Ru-106. By employing gold blocker, low-energy plaques deposit energy in an isotropic way

with a higher dose gradient, so that the surrounding normal tissues are spared to enhance the safety.

Currently, a bowl-shaped, gold-eye plaque with I-125 seeds is the most commonly used setup in North America for the brachytherapy of uveal melanomas. However, there are alternative sources instead of the I-125 for brachytherapy. In Europe, plaques with isotope Ru-106 (ruthenium) seeds are common options for most uveal melanoma treatment. Radioactive gold (Au-198) and palladium (Pa-103) as seeds have been reported as well [13,32,33]. A dosimetric comparison study [39] of Ru-106 and I-125 plaque brachytherapy for treatment of the shallow small choroidal melanoma lesions was based on 26 consecutive patients by using plaques with the diameter of 16mm, 18mm, and 20mm respectively. The results showed that the I-125 plaques introduced a higher sclera/apex dose with respect to the height of apex; two dimensional dose distribution and dose volume histograms demonstrated the increase in dose outside the tumor volume, while the Ru-106 plaque presented a much more conformal dose distribution. This suggested that Ru-106 is a potential isotope candidate to spare the surrounding normal tissues and to reduce the risk of radiation complications.

Regarding the palladium-103 isotope, one study [26] was conducted upon 152 patients with uveal melanoma and negative to metastasis. The Pd-103 plaques were sewn to the episclera to cover the base of the tumor with dose prescription of 80.5 Gy/5-7 fractions. After a mean 4.6 years follow-up, the performance of Pd-103 was equivalent to the I-125 in terms of the local tumor control, but better with respect to the visual acuity.

A retrospective study [31] from British Columbia Cancer Agency focused on the effects of the Au-198 plaque brachytherapy of 79 patients with primary choroidal

melanomas. The Au-198 embraces a half life time of 2.7 days and emits majority gamma rays with energy of 412 KeV with a half value layer of 3mm of lead. The analysis from 77 patients demonstrated that the free survival rate and the local actuarial local tumor control is 94% and 98% respectively in the case of the 5-year actuarial enucleation; the actuarial disease specific survival rate is 95%; and 78% of the patients achieved a better visual acuity in the case of brachytherapy. The paper concluded that the Au-198 plaque brachytherapy for the choroidal melanoma reached an excellent survival rate and local tumor control with minimum significant toxicity by preserving the globe and the result was comparable to other outcomes by employing different isotopes, such as the I-125, Co-60 and the Ru-106.

A reanalysis [25] of the eye plaque dosimetry for the medium tumor from COMS indicates that a significant and consistent reduction of doses to the critical tissues can be reached by incorporating the anisotropy, line source approximation and gold attenuation into dose recalculation.

Detailed biological effects of plaque radiotherapy of uveal melanomas have been published in literatures in addition to the introduction from Chapter 1. Since most ocular tumors appear in the posterior chamber, the complications [3, 11, 32-33,47-50] come up with the influence to the posterior tissues or indirect anterior side effects. It involves the cataract, the proliferative radiation retinopathy, the maculopathy, the neovascular glaucoma and the exudative tumor response. Studies indicated that the plaque brachytherapy is recommended for the small progressing choroidal melanomas, the medium posterior melanomas and the large-sized ones for an only eye.

In summary, the brachytherapy, as the original type of external beam radiotherapy of ocular tumors, especially uveal melanomas, has demonstrated the effectiveness for the local control with comparable or lower recurrence rate, and mobility rate. Different impacting factors for the brachytherapy have been investigated in literature, such as the radioisotope and plaque blocker. But the experience of pain and uncomfortableness introduced by general or local anesthesia, the accompanied surgery and the left scar are undesirable for patients.

2.5 Transpupillary Thermotherapy

Hyperthermia has been employed to heat the designated tumor volumes accurately and uniformly via the specific equipment. The biological effect presents in an opposite way compared with the radiation. First, the irradiated cells die only in attempting the next or the subsequent mitosis, whereas the death of heated cells and the heat damage show up earlier. Second, the cells in an acid pH environment and deficient in nutrients appear to be heat sensitive, but present radiation resistance. So the combination of heat and radiation therapy will complement each other, and the therapeutic gain is reduced by lowering the radiation damage to the normal tissues eventually.

In the case of uveal melanomas, hyperthermia treatments become available in the form of transpupillary thermotherapy (TTT), laser photocoagulation (LP), the combination of brachytherapy with TTT or LP, or the combination of proton radiotherapy with TTT, etc.

The transpupillary thermotherapy alone [3, 11, 13, 16, 40-46] has been attempted to induce the heat necrosis of uveal melanoma to temperature of 60-65 degrees by deploying an infrared laser beam with a wavelength of 810nm through the dilated pupil in one or more

sessions. A similar technique, the laser photocoagulation, is used to reduce the damage to the retina by employing a sector scatter laser. On the other side, complications along with the TTT involve the scotoma, macular traction, vascular occlusion and the hemorrhage. As a primary treatment [44], a relatively high recurrence is found in a range of 23% to 45%. It is only limited to the small melanomas due to the ability to penetrate thick tumors. With respect to the long-term choroidal vascular changes, a comparison between the iodine brachytherapy (IBT) and the TTT for the small choroidal melanoma [45] demonstrates that TTT is less effective in closing all tumor vasculature. Currently, TTT serves as a complementary or secondary treatment with brachytherapy or the local resection to kill the tumor and spare the normal tissues to the maximum degree. The combination of the proton beam radiotherapy and the TTT for the large uveal melanoma [43] demonstrates a significant decrease in the secondary enucleation rate. A five year study [42] shows that the combination of the Ru-106 brachytherapy and the TTT for choroidal melanoma delivers a bitter-sweet message of a low rate of recurrence accompanied with considerable loss of visual acuity.

Literatures show that the hyperthermia treatment for uveal melanoma, such as the TTT or the laser photocoagulation, is restricted to a secondary complementary way to radiotherapy or the surgical enucleation.

2.6 Proton Beam Radiotherapy

The proton beam is a form of charged particle beams. The charged particle radiation [3, 11, 51-56] was attempted in the early 1950s by its dosimetric advantages in terms of the accurate energy deposition. The proton beam energy increases as the depth reaching to the Bragg peak, where the maximum energy is deposited near the end of the

beam range and the dose drops rapidly after the distal falloff. This property enables a high precision conformal energy delivery to the tumor volume and keeps the normal tissues out of the range of Bragg peak for the sake of protection.

However, the proton beam radiotherapy requires specific procedures. First, the general workflow involves the surgery operation. Before the charged particle beam radiation, the tantalum clips are sewn to the episclera around the base of the tumor so as to localize the targeted region. This imposes pains to patients and requires experienced skills for surgeons. Second, it is an expensive investment to build a proton facility. Regarding the generation process, negatively charged hydrogen ions (1 proton and 2 electrons) are generated from an ion source, which are transported through an evacuated electrostatic beam line to a high energy (500 MeV) cyclotron. Then the focused and accelerated ion beams are transferred into a magnet system to remove the electrons. Eventually the protons are preserved and deflected out of in the magnetic field. Currently, there are only around one dozen hospitals capable of offering the proton beam radiotherapy. Around ten are under construction in the USA. It costs more for the equipment and requires more space to accommodate them, which is not as easy and convenient as the process to obtain the radioactive beam, electron beam or photon beam from radionuclide or the LINACs. Thus, the availability of the proton beam treatment for uveal melanomas patients still waits to be pushing up.

In published literatures, few restrictions are reported for the proton beam radiotherapy of uveal melanomas with respect to the size and the location of a tumor. In general, it is adjustable for any tumor size, but not recommended for large tumors taking more than 30% of the ocular volume. A five year proton radiation therapy [54] of the medium and the large

choroidal melanoma testified that it was a safe and effective way to preserve the eye. Another paper [56] investigated among 2568 uveal melanoma patients, 20% are small tumors, half of them are medium tumors, and the rest 30% are large tumors according to the categorizing from COMS. It concluded that the proton therapy is a preferred option for the peripapillary tumors. A study [43] with the combination of the proton beam radiotherapy and the TTT for large uveal melanomas has been attempted among 151 patients. The result shows that a significant decrease in the secondary enucleation rate in patients who were treated with the TTT after the proton beam radiotherapy under a comparative condition that half of the patients received the proton treatment with 60 Gy in 4 fractions and the other half followed by extra TTT. The outcome showed a significant decrease in the secondary enucleation rate in patients treated with TTT after proton beam ratiotherapy. Different from the brachytherapy, most side effects of the proton beam treatment occur in the adnexal and anterior chamber, including symptoms of dry eye, iris neovascularization, ididocyclitis, corneal ulceration, posterior subcapsular cataract, radiation maculopathy and papillopathy, etc. This is determined by the irradiation direction.

In summary, the precision targeting enables the proton therapy standing at a competitive position with the accurate dose delivery. On the other side, the practical availability of the proton beam modality is restricted due to the high expenditure and the complicated process to generate charged particles.

2.7 Gamma Knife

The concept of “radiosurgery” was introduced by Lars Leksell in 1951, a Swedish physician. The first prototype of the Gamma Knife was installed in 1968. Leksell Gamma

Knife is named after its inventor. This type of stereotactic radiosurgery was originally designed to treat the brain tumors, vascular abnormalities, skull tumors and the neurological functional diseases with high precise dose delivery.

The Leksell Gamma Knife [57-66, 93] is a frame-based treatment modality to focus the overlap or the coverage of multiple radiation beams on a relatively small tumor volume. The dose is delivered by around 201 Cobalt sources distributed on the surface of a hemisphere dome-shaped helmet to collimate to a focal point in a target. A special lightweight aluminum head frame with a built-in 3D coordinates is attached to the skull. The targets are treated by "shots", a combination of beams. The Gamma Knife radiosurgery is accomplished through the imaging simulation, the planning and the treatment execution, as an usual routine for the SRS/SRT.

In the case of uveal melanomas, the result [60] from a twelve year experience of the Gamma Knife radiosurgery based on 78 consecutive patients with a dose level of 30-50 Gy, indicates that the Gamma Knife treatment can be a candidate for the choroidal melanomas instead of enucleation. Another paper [58] based on 58 patients with the unilateral large uveal melanomas treated with the Gamma Knife shows that 97% of patients reached the local tumor control; tumor height decreased by 33% in median value; and tumor volume decreased by 37%. But the higher complication rates compared with the proton beam radiotherapy and the plaque brachytherapy is reported due to the difficulty to deliver the fractionated dose with a frame-based modality.

In conclusion, the Gamma Knife offers precise dose delivery by virtue of the hemisphere design and the high tumor local control in clinic, but patients cannot avoid painful procedure for the fixation of the rigid helmet before a surgery.

2.8 LINAC based Radiation Treatment

The LINAC is regarded as a form of linear accelerator to produce radiation beams. It generally utilizes either the klystron amplifier or the magnetron to produce electrons, which are accelerated through the waveguide structure. The beams come out of a gantry rotating around an isocenter, which is the focus of the patient on a therapeutic couch.

The beams could be electron beams or photon beams depending on whether the electron beam applicator is setup or not in the machine. In general, the energy of photon beam is at 6MeV or 23MeV, and that of electron has different levels, from 6MeV, 9MeV, 12MeV, 16MeV till 23MeV. The photon beams are applied to a relatively deeper location inside the body, while electron beams are easy to deliver higher dose on the surface of the patients. To compensate the energy distribution around the target, varieties of accessories are employed, such as the bolus, the photon block, the electron cutout, the compensator, the dynamic wedges, and the multi-leaf collimators, etc.

Treatment techniques based on LINACs have been developed from the original conformal planning to the intensity modulated radiotherapy (IMRT) and the volume modulated arc radiotherapy (VMAT). The aim of these techniques is to cover a complicated target volume and to reduce dose to the normal tissues by the trajectory dose line with the help of dynamic shaping facilities (wedges, MLC) within a comfortable time period for each fraction.

Frameless is an evolved advantage for the LINACs compared with the framed treatment, such as Gamma Knife. A noninvasive thermoplastic head immobilization system underwent research in the middle of 1990s, which was designed to reproduce the position during the simulation and treatment to the maximum degree. It doesn’t need

bone fixation, and easy to get into shape quickly. The mean axial displacement for the repositioning was 0.6mm. The frameless radiotherapy is applicable to the brain tumor with the help of the thermoplastic mask, and other parts of the body (i.e. the spine, lungs and abdomen with rhythmic movements, the superficial skin tumor, lymph nodes, and the orbital tumors etc.) with the assistance of other forms of immobilization devices.

In literature, studies [67- 73, 93] report that the treatment of uveal melanomas with the LINAC based SRS/SRT have been attempted. A paper [68] depicting the malignant primary choroidal tumors with 10 metastasis and 5 primary cases under different prescription around 20Gy for metastasis patients and 50Gy/10fractions, was deployed and validated by the visual acuity of patients. The outcome included the successful local tumor control for all patients, 8 of 15 patients achieved the tumor regression, and no persistent side effects were observed for a follow-up from 1 to 34 months. This study demonstrates that the SRT allows the steep dose gradients outside the target volume by minimizing the field of exposure and suggests it may be effective in controlling the tumor growth. Regarding the impact of the fractionated SBT of choroidal melanomas from the small to the medium size, a study [70] based on 102 uveal melanoma patients with 32 months follow-up reports that patients underwent the treatment with the help of a non-invasive relocatable Gill Thomas Cosman stereotactic frame and with dose prescription of 50Gy/5 fractions. The result showed the majority (96%) patients obtained the local tumor control, and a 5-year actuarial metastasis free survival was 75%, which is comparable with the similar cases treated by the proton beam. therapy Although complications including the progression (4/102), the toxicity (9/102), the neovascular glaucoma (8/102), the retinal detachment (1/102), and the endophthalmitis after

vitrectomy(1/102) happened, the total effect shows that this technique could be a potential approach for good local control and sparing normal tissues as the same time. As advanced IMRT is concerned, the treatment planning [71] of forty uveal melanoma patients was compared between four techniques: conventional arc, static conformal, dynamic arc plan and IMRT. It turns out IMRT offered the benefits to reduce the dose to the lens but not for the optical nerve, and IMRT could be an option for the treatment of uveal melanoma.

In summary, the LINAC-based stereotactic radiotherapy has become an effective way to control the small and the medium sized uveal melanoma and partially spare the normal tissues around the target. The intriguing aspect is the characteristic of frameless, which adds no extra pain to a patient. However, the issue comes up to the immobilization of the head and the diseased eye. Thermoplastic mask is a solution for most head and neck cases, but is not sufficient for the treatment of the ocular tumor, such as the uveal melanoma. As an option, the next section offers a form of image-guided radiosurgery.

2.9 CyberKnife (Robotic Surgery)

The gantry-based dose delivery technique (LINACs) permits the frameless radiotherapy compared with the Gamma Knife treatment with a rigid frame. However, the gantry-based system only allows the gantry movement in one plane, even with the compensation of the additional couch movement. On the other hand, the rotation of couch is potential to introduce the alertness, nervous and unsafety of patients during the treatment.

This issue is solved by the CyberKnife machine, the pioneer of the combination of the robotic operation and the radiosurgery. It is a product from the Accuray to deliver the

ionizing radiation beam precisely and accurately by employing a real time frameless image-guidance and six-degree of robotic positioning to overcome both geometrical limitations for the dose delivery in the case of the gantry-based systems and the invasive aspect of the frame-based stereotactic systems.

The CyberKnife system benefits from the robotic arm and is characterized as a sensor-based application to perform the precise and versatile actions under some specific conditions. This feature brings the flexibility for the beam delivery. The CyberKnife system currently utilizes the photon beams with energy of 6MeV, generated from a linear accelerator mounted on the robotic arm. The machine can work with one single isocenter, multiple isocenters, or completely non-ioscentric. The beams automatically go over between paths, composed by different nodes pointing to the target volume, by following the treatment plan. It has the advantages of knifeless, frameless, bloodless, no tissue loss, non-invasiveness, and avoiding side effects from the traditional surgery, such as infection, swelling of tissue. The general anaesthesia is not necessary for the patient, therefor the anaesthesia related morbidity and mortality vanishes at all.

The CyberKnife stereotactic radiosurgery [74-80, 93] belongs to an image-guided operation. The imaging simulation (CT, MRI or PET) is the initial step, which demands a higher resolution to provide more accurate information for the treatment planning and the treatment. During the treatment stage, two invisible orthogonal films on the ground receive the x-ray images in real time and register with the DRR (Digital Reconstructed Radiograph) to determine the couch correction parameters relative to the tumor center. The latest corrections are transferred into the robotic command lists to adjust its next movement. In general, the bony landmarks are good for registration. The implanted

fiducials are an alternative way to determine the corrections when the bone doesn't dominate, such as in the soft tissue, the lungs and the prostate. In terms of the regular movement, CyberKnife has a synchromantic protocol to track the respiration with infrared reflector and acquires the gated images as guidance. This could happen to the lung tumor or the liver tumor. Another feature of the CyberKnife is the high dose delivery to targets in few fractions to perform radiosurgery. In this way, it saves much more time for patients compared with multiple fractionated radiotherapy treatment.

In the case of uveal melanoma, the frameless treatment follows a thermoplastic mask-based procedure for head and neck plus expanded techniques to deal with the fixation of the eye. Some studies [81, 82, 94] have been attempted but lack of statistical summary of the outcomes for ueval melanomas treated by the CyberKnife. For instance, five patients with the medium-sized uveal melanoma and the juxtamacular tumors were treated by the CyberKnife in a fractionated dose of 20 for three fractions. The eye was stabilized via the injection of lidocaine. The result [82] showed a remained stable and improved vision and the decreased thickness of the tumor for an eight months follow-up without serious acute side effects. Another paper [81] assessed the performance of the CyberKnife radiosurgery of the intraocular and periocular lymphoma based on 13 patients with 14 eyes with a mean dose of 17.18Gy/5 fractions over a mean follow-up of 23 months. It outcome included: 2 patients with dry eye, 1 patient with cataract and conjunctival lymphoma, no report of retinopathy or palillopathy and the visual acuity was preserved or improved in 13 eyes.

In summary, the CyberKnife demonstrates the advantage in terms of the frameless, the flexible robotic arm and the fractionated high dose delivery. It possesses the potential capability for the treatment of uveal melanomas.

2.10 Comparison of Radiosurgery/Radiotherapy of Uveal Melanoma

All methods discussed above are listed in the following table for feature comparison.

Table 1: Comparison of radiosurgery and radiotherapy techniques for treatment of uveal melanoma

	Plaque Brachy-Therapy	TTT	Proton Radiotherapy	LIINAC based SRT/SRS
Tumor Size	Small, Medium	Small (primary tumor) Medium/Large (Secondary)	Small, Medium Large(+TTT)	Small, Medium
Treatment Duration	Isotope half life time			20-40 min SRS; 10-30 min SRT;
Local Tumor Control (LTC)	91% (5 yr)		>90%	90%
Resurrection	12%(IBT); 4%(IBT,5), 11%(Ru,5); 1.7%(IBT,careful placement);	3%(5, IBT+TTT);	5%(5)	
Complications	Posterior chamber; Retinopathy; Papillopathy; Cataract; Vision decrement; Vitreous hemorrhage; Neuropathy;	Retinopathy, scotoma, mascular traction, vascular occlusion and hemorrhage	Adnexal and anterior chamber, including dermatitis, eyelid edema, bleppharitis, keratitis, conjunctivitis, iridocyclitis	Toxicity; neovascular glaucoma; retinal detachment;

	Neovascular glaucoma		(acute); Eyelash loss, dry eye, corneal ulceration, iris neovascularization, secondary glaucoma, cataract (late)	
Stereotactic	No		Yes	Yes
Frame			Frame	Frameless
Fractionation	No		Yes	Yes
Invasive	invasive	invasive	invasive	noninvasive
Advantages	Effective way to control and treat uveal melanoma; High dose gradient by ru106, i125, pd103;	Effective in closing tumor vasculatures;	Bragg peak, high dose gradient; Accuracy; Conformal dose; No dose to contralateral OARs;	Conformal dose, especially IMRT, VMAT; Robotic couch; Infinite source of photons; Fractionation; High dose gradient; Sparing normal tissues;
Disadvantages	Surgical affixing of plaque containing isotope sources on the base of the tumor; Potential metastasis;	Limited to small sized choroidal melanoma;	Restricted modalities;	Cannot eliminate dose to contralateral OARs;

Table 1 continued.

	Gamma Knife	CyberKnife	Enucleation
Tumor Size	Small, Medium	Small, Medium, Large	Large
Treatment Duration	Depends on Co HL	SRS (40-60 min); SRT(30-50 min);	
Local Tumor Control	90%		

(LTC)			
Resurrection	SR>80% (3-5)		3%(5), 4.2%(10), 4.8%(15)
Complications	exudative retinopathy, neovascular glaucoma, radiogenic retinopathy, vitreous haemorrhage;	Dry eye; Cataract; Retinal detachment	Metastasis
Stereotactic	Yes	Yes	
Frame	Head Frame	Frameless	
Fractionation	No	Yes	
Invasive	Invasive-soft tissue marker	noninvasive	
Advantages	Ideal for functional lesioning; Minimal preventive maintenance; Simple quality assurance	Versatility in treatment planning (isocentric or nonisocentric); Higher daily patient volumes; Infinite source of photons; Fractionation; More dose homogeneity;	Removal of progressive large ocular tumor;
Disadvantages	Co reload; Co decay a variable dose rate; Geometric constrains of fixed frame application; More limited patient base; lower daily patient volume (5-7/d)	Longer treatment times with lower output; More preventive maintenance; More quality assurance;	Metastasis;

2.11 Eyeball Immobilization for Noninvasive Treatment

The unpredictable eyeball movement during the radiation surgery imposes risks for the surrounding normal tissues, and uncertainty for the treatment planning. This requires the application of the eyeball immobilization to eliminate the relative movements regarding the skull. Several experimental settings have been investigated from this stand point [58, 74].

One of them is anesthesia. It becomes a prevalent option in clinic to freeze the eyeball during treatment. However, sometimes the repeatability to keep the eyeball as the same location for both the planning and the treatment stages is questionable. Furthermore, the patients do feel uncomfortable when they get awaken again. Next, the alternative schemes step up instead of the medicine solution. For instance, the suction device can fix the eyeball from moving in a certain range, but at the high risk of damaging the anterior segment. Another choice is to implant tantalum clips, sewed on the sclera during the proton therapy, which requires an invasive painful surgery operation.

On the other hand, the research on the eyeball immobilization devices diverts into another direction: the noninvasive fixation. This type of device [68, 72, 83-87, 89-90] usually includes a mechanical setup, a light guidance and a monitoring camera according to literatures. The mechanical part could be attached to the treatment couch, on the mask or to the stereotactic frame. The light source could be a blinking source or a static one. The camera tracks the eyeball movement; the paired software extracts the 2D image features and serves as an alarm for the beam control.

In literature, certain specifically designed noninvasive immobilization devices are desirable to meet the clinical expectation. They distinguish themselves by the treatment modality, main components, and the arrangement of those components.

In the application of the CyberKnife radiosurgery, Daftari's [83] group introduced two easily adjustable plastic arms mounted on the treatment couch, attaching to a mirror and a light source, respectively. The LED light source guides the patient's eye for the fixation. On the other arm, the mirror reflects the patient's eye. The mounted CCTV camera

captures the reflected image from the mirror for monitoring. Once the pupil is observed out of a tolerance range of 0.5 mm from the original center, the beam is turned off.

A similar monitoring system is reported by employing a camera in a different setup arrangement. The LINAC-based stereotactic radiotherapy of uveal melanoma [85] is complemented by employing a thermoplastic mask frame to fix the patient's head first. A hollow plastic tube mounted on the frame is designed to contain the camera cable and transfer the yellow LED light to the other end point - the closest location to the diseased eye. Therefore, the metal parts in the camera will not influence the CT or MRI imaging.

Regarding the fixation mask, another group [68] developed an individual mask, tightly attached to the stereotactic frame. A flashing point is used to direct the patient's eye in a similar way during the treatment. The same position could be reproduced during planning and the treatment stage. Here the corneal reflection of the flashing light is explored from the captured images in addition to a simple function for monitoring. Another point is the adoption of a flashing light source, instead of the static one.

One specific re-locatable stereotactic frame [84] for the irradiation of eye melanoma is constructed by a plastic frame, a blinking light source and a camera. The flashing light is delivered through the fiberglass connected to a light-emitting diode and positioned in front of the normal eye; the small camera is positioned in front of the affected eye for checking and monitoring.

Another group [90] engaged in an eye tracking and gating system for the proton therapy of orbital tumors. They attached the LED light source on the proton beam tube to guide the eyeball fixation; the patient's eye was captured by an infrared CCD camera. The camera monitored the eyeball movement to trigger a warning message for the

suspension of the proton beam as the eye is out of acceptable range. The paper also introduced a calibration procedure to determine the ratio of the actual distance to the pixel distance for surveillance.

Next, a type of setting [86] assembled the fixation device based a Brown-Roberts-Wells head-ring. It employs a goggle without the plastic glass to stick to the patient's skin as one arm of the "U" frame. On the other arm, a special LED source was adapted to the patient's view surrounded by a black rectangular piece of soft foam to increase contrast of the light source. During the radiosurgery, an infrared TV camera was mounted next to the light spot to monitor the eyeball movement.

In summary, the light source (static or blinking) was employed as a trigger to fixate the patient's eye, either the healthy one or the diseased one. This approach is effective to guide the patient's eye and keep it stable in a smaller range. The CCTV or normal spectrum camera serves as a monitor to check whether the pupil or other landmarks on the image deviating out of the valid range or not, so as to control the irradiation beam. Some groups dig further and developed their own contouring algorithm and software to identify the pupil location.

However, the role of the camera is limited to monitoring by the therapists. It implies there is a break time between the human recognition and the execution of beam control. In addition, it takes a response time as well for the therapists to make decision. Besides, the human factor is unavoidable, because there might have different responses from different observers for the same signal. In addition, the normal light camera is easy to be influenced by the environmental light. All of these impose challenges for the detection of the eyeball movement by human naked eye or automatic recognition.

Chapter 3 Optical Tracking System

3.1 System Description

As discussed in the last section of Chapter 2, noninvasive radiation treatment of uveal melanoma has become an attractive field to eliminate ocular tumors and reduce patients' pain to the maximum degree. This concept leads to the adoption of a tracking camera. Traditionally, the camera can achieve the purpose to monitor the eyeball movement observed. Eventually it is the therapist's task to decide whether the beam should be on or off by the reference from the camera image. Moreover, no study has shown the connection between the pupil position in the live camera image to the corresponding 3D tumor location by the aid of any image-guided radiotherapy or radiosurgery modality. This turns out to be the original motivation for this dissertation, which is to build a guiding system for the robot arm of the CyberKnife system with regard to unpredictable eyeball movement, so that the live tumor location will become a live input to the CyberKnife system by taking advantage of the tracking infrared camera.

In our tracking system, the framework evolves from the original transformation algorithm to obtain the 3D tumor location and upload to the radiosurgery machine for real time adjustment. Next, the key hardware components are developed and integrated together to pull through the innovate idea. Validations of the algorithm and integrated system are completed comprehensively to bring solid feasibility for clinical trials and application. Technically, any radiosurgery modality that can offer real time image guided operation will benefit from the system, such as the CyberKnife or the proton beam therapy. In particular, the eyeball fixation device could be optional by only employing the tracking in clinical treatment, or could be a necessary component due to clinical

requirements. If necessary, it also might be possible to develop a similar noninvasive eyeball fixation device for better performance. The task of this dissertation is focused on the establishment of the original 2D/3D tracking algorithm and the validation phantom system, as shown in Figure 1 and Figure 2.

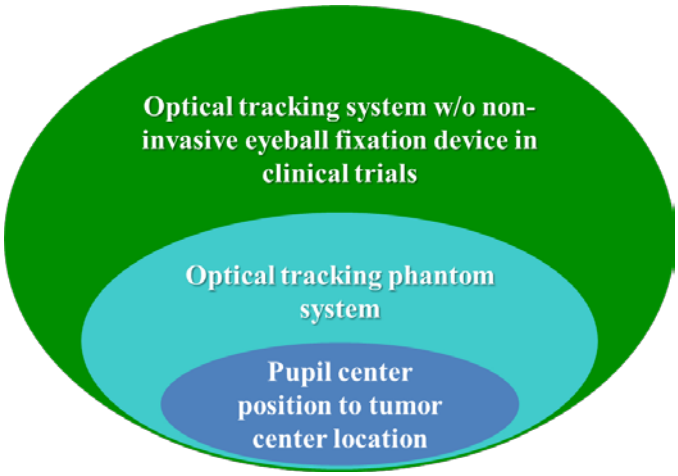

Figure 1: The Roadmap of the development the Optical Tracking System

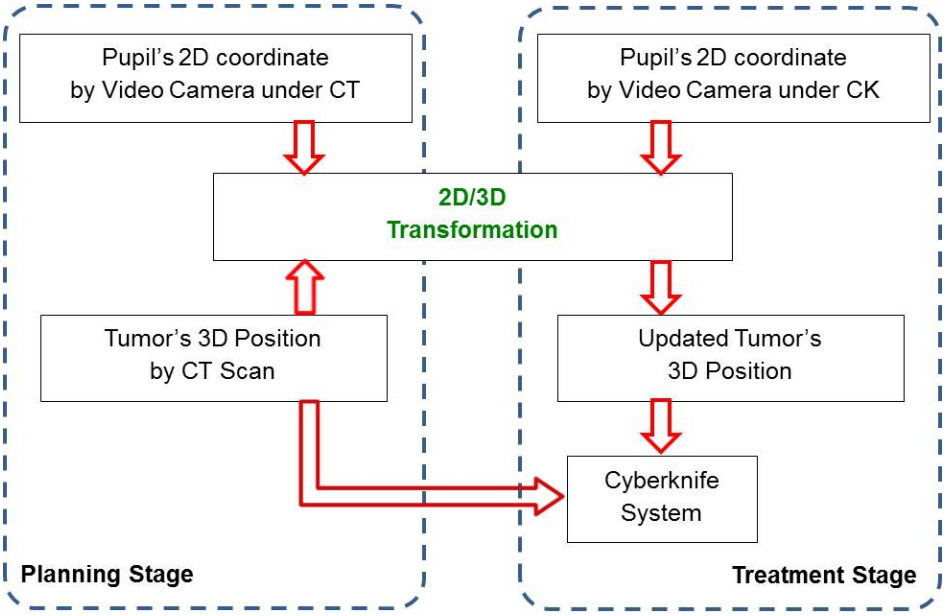

Figure 2: The Main Chart Flow of the System

The main flow chart in Figure 2 shows two procedures with one shared operation. The CT planning stage and the clinical treatment stage, both of them adopt a derived 2D/3D transformation algorithm. During the CT planning, four pupil corner extreme positions are acquired by the camera and the corresponding 3D tumor locations are obtained from the corresponding CT DICOM data. Based on these data, it is sufficient to calculate the 3D tumor locations by applying the 2D/3D transformation algorithm. Thereafter, the error distance between the calculated value and the measured value from the DICOM file can be used to evaluate the performance of the phantom system. Similar calculation and error analysis can also be applied to the CyberKnife treatment stage. Besides, there is little difference regarding the CT calibration and the CyberKnife calibration. The calibration for the CyberKnife is obviously to obtain the tumor center locations that will be uploaded to the robotic arms during the treatment, when the estimated error distance stays within a tolerance. However, regarding the CT simulation scanning, the predicted error distance could serve as a threshold to determine whether it is feasible for the CyberKnife treatment. If not, it calls for the root cause analysis to uncover the reason and solve the problem.

The connection between the CT planning and the CyberKnife treatment comes up as the initial alignment in the CyberKnife system at the neutral pupil position. In another sense, it is necessary to repeat the same neutral position in the CyberKnife experiment as that from the CT test. This step is crucial, because the origin point shifts to the tumor center under the CyberKnife coordinates.

In terms of the execution of the phantom system, this includes communications and cooperation between components as shown in Figure 3. The hardware includes: the

commercially available infrared tracking camera, the eyeball phantom, the eyeball holder, the extensible module, the linear stages and the main frame. The Software simulation and the communication with the camera platform are integrated as an in-house application. Together with the control software for the linear stages, they constitute the so-called control console as shown in Figure 3. The outcome presents an updated 3-dimensional simulated eyeball and the coordinate parameters displayed in the control center, which is corresponding to the rotated plastic eyeball phantom driven by the linear stages controlled by the console center. Another outflow from the control console belongs to the uploading process to feed the predicted tumor center location into the CyberKnife operation system.

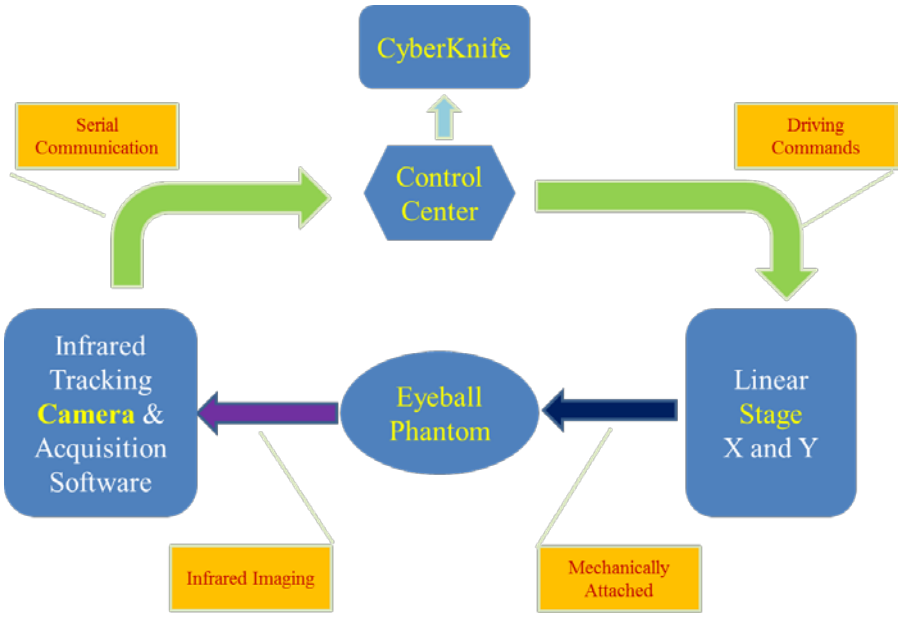

Figure 3: The Workflow of the Phantom System

3.2 Calculation Workflow

This section aims to explain the computer simulation process in details. Across Figure 4, the system calibration and the inverse transformation are intermediate steps between the input in the form of the pupil center, the tumor location and the output in terms of the tumor location and the related update.

The first step of the calculation workflow needs to interpret the 2D pupil position into the counterpart 2D deviation for the tumor, so as to constitute the genuine paired tumor data set. This transformation also relies on the rigid phantom by applying a scaling adjustment between the eyeball radius and the offset of tumor center from the spherical origin. At the same time, the same ratio exists between the pupil center offset and the corresponding tumor deviation. In this way, the pursued tumor deviation can be obtained.

The next step picks up the calibration resolution, which is the outcome of the system calibration. It represents the procedure to obtain the ratio of the pixel distance from the camera images to the real distance from CT DICOM data and the CyberKnife data. Four marginal calibration positions and one neutral position are designed. As an intermediate outcome, two crossing perpendicular lines are constituted by the four margin points in terms of the 2D pupil center. They are supposed to be paralleled or very closely paralleled to the vertical and the horizontal axis on the 2D image plane. Regarding the 3D measurements, two corresponding projected distances coming from the tumor locations are gathered through a simple transform. This step rules out the participant of the Z value due to the projection to the plane XoY. Therefore, the resolution ratios along two axes can be obtained. Under the ideal imaging circumstances, the two ratios should be equal to

each other. However, by taking the camera angle's influence into consideration, the horizontal and the vertical ratios may become different.

The inverse transformation can find the ground truth of the tumor center for an absolute neutral pupil positioning, because this location serves as an initial parameter to perform the 2D/3D transformation. In reality, it is difficult to put the eyeball in the perfect position so that the pupil center coincides exactly with the image center during experiments. According to the transformation equation (Table 2, Section 3.3), the inverse transformation can be fulfilled with any paired, recorded, 2D and 3D dataset. To minimize the system error, this pair data set is assigned to the recorded neutral pupil position and related tumor center from the DICOM file. In this way, the ground truth neutral tumor location is evaluated.

After this preparation, the dynamic input in the form of the pupil center together with the prepared calibration resolution can be transformed into the 3D tumor location. This scenario can be interpreted through the visualized dynamic eyeball simulation. Detailed 2D/3D transformation will be unfolded in the next section. The execution of calibration during CT and CyberKnife experiments will be introduced in Chapter 5.

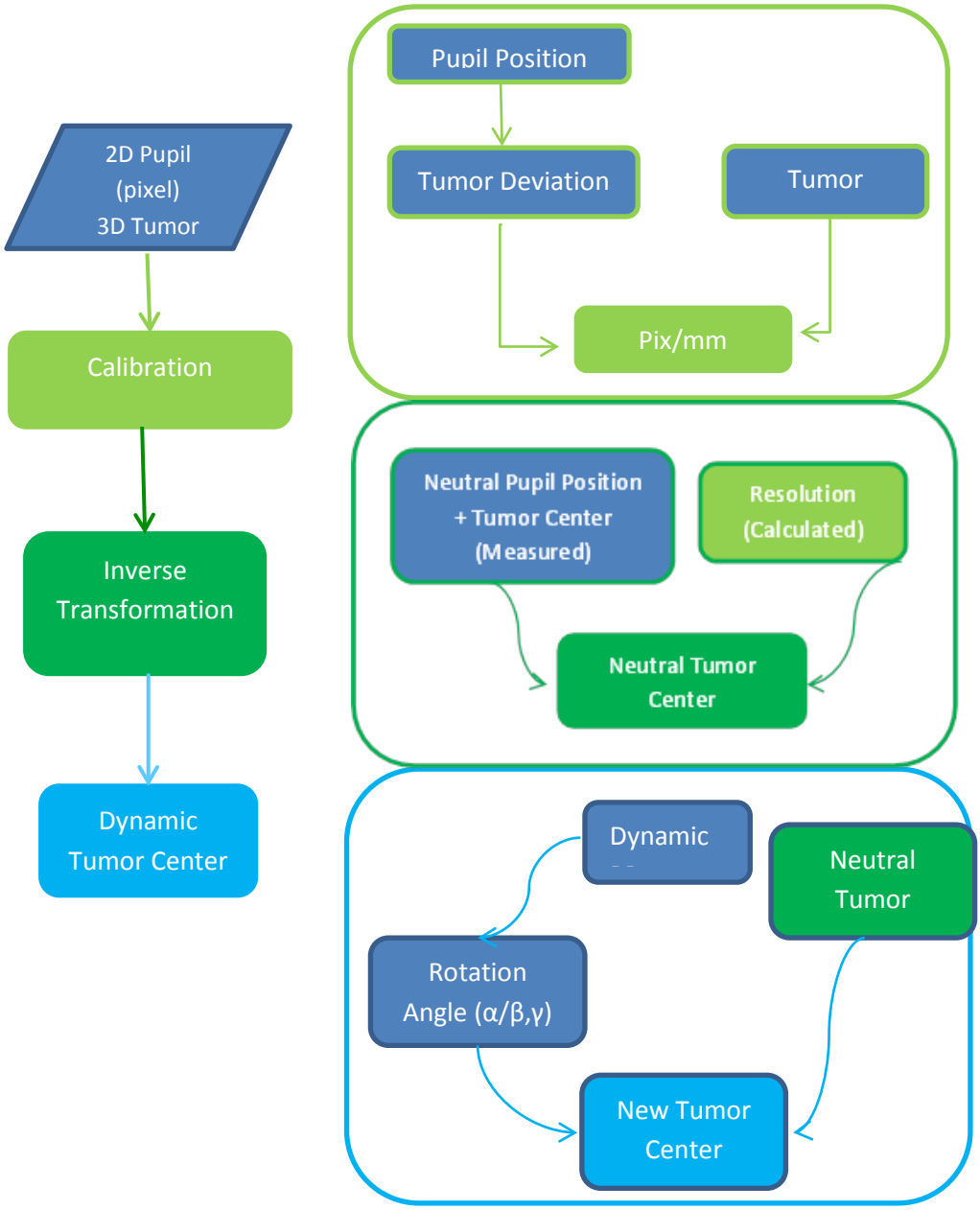

Figure 4: The Flow Chart of Calculation and Calibration

3.3 2D/3D Transformation Algorithm

We propose a 2D/3D transformation algorithm to get the tumor location from the camera image based on a rigid eyeball module. Since the patient's head is fixed during treatment, the third rotation along anterior-posterior axis is limited based on the Donders' law. On the other hand, the unexpected rotation implies a multiple to one mapping

between the pupil center and the tumor location, which is an abnormal physiological phenomenon. Another concern is the eyeball translation in the orbit, which is relatively negligible, and the impact can be explained in the error analysis section. Therefore, the outcome of the eyeball movement is simplified to by rotating along the horizontal axis and the vertical axis and by ignoring the eyeball translation in the orbit. The 2D/3D transformation matrix only includes rotation parameters around the horizontal and the vertical axis for this specific study [1-2, 91].

The geometric rotation angles are responsible for the connection between the 2D pupil center and the 3D tumor location. However, no literature studied the connection between the pupil deviation and tumor center. For instance, some paper mentioned the relationship between a rotation angle and the path on the surface of the eyeball. One study has introduced this relationship to estimate the coverage of PTV (Planning Target Volume) after a deviation of pupil from the center. By assuming the eyeball diameter of 22mm, the pupil deviation of 1 mm will introduce globe rotation with 5 degrees, which still hold the GTV (Gross Target Volume) covered by 80% of the original isodose of the PTV according to 94% of the measurements [72]. The translation of the eye position between planning CT scan and the verification CT scan was related to the rotation angle of the eye globe. This was pointed out in a paper [84].

As illustrated in our published paper [92], the goal is to derive the geometric relation and make it feasible to obtain the 3D tumor location from the pupil position. It is based on a rigid system, and the sphere is chosen for the convenience of interpretation. Here we define the sphere center as the coordinate origin. The first step is to drive the geometric relationship between the 2D position and the rotation angle. The next step applies this

transformation to a designated pupil position. Eventually, the tumor center is obtained with the help of the calibration resolution to set the unit in terms of millimeter.

As the eyeball is simplified as a spherical ball, the following deductions in the 3D coordinate system are oriented to the eyeball center. Suppose the end point (**P**) of the vector ***oP*** on the surface of the spherical with the radius R is the interest point. It projects to the plane ***MQN*** as ***QP*** comprising the point **P**, to the plane ***XoQ*** as ***oa***, to the plane ***YoQ*** as ***ob***. The angle **α** is formed in the plane ***XoQ*** as ***Qoa*** or ***Zoa***, **β** is introduced in the plane ***YoQ*** as ***Qob*** or ***Zob***, and **ϕ** sits in the plane ***PoQ*** as ***QoP*** or ***ZoP***.

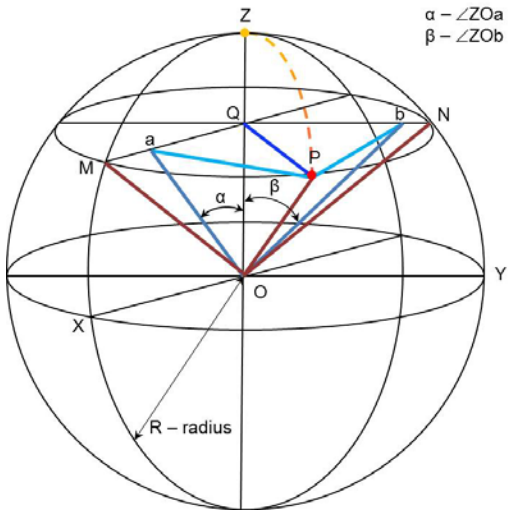

Figure 5: The Geometry of the Eyeball Sphere

As the above conditions are clear, the 2D picture (Figure 5) is obtained as the top-bottom view of Figure 6. The point **o** and point **Q** overlap at the same position. The segment ***QP*** has the projection ***Qa*** and ***Qb*** at the axis ***QM*** and ***QN*** respectively. The plane ***QMN*** owns a radius of **r**, which can be calculated from the projection ***Qb*** and ***Qa***. This view is to simulate the camera tracking in the real experiments.

The front view and side view (Figure 6) could be the plane ***ZoX*** and ***ZoY***, with the angle **α** and **β** coming from ***Zoa*** and ***Zob***. The spherical radius (**R**) and the radius of plane ***MQN*** (**r**) constructs a right triangle, which is used for further calculation.

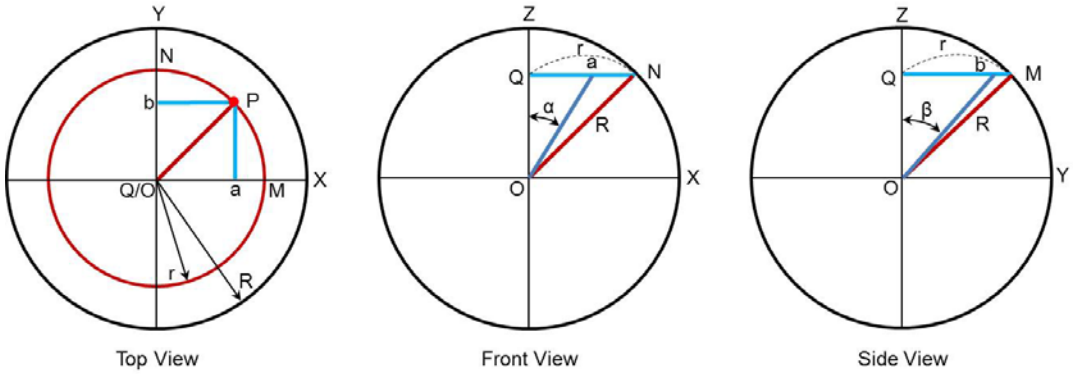

Figure 6: Different Views of the Sphere Eyeball

Till now, the requirements to obtain the rotation angles are settled down and the calculations are listed in Table_1. The radius of **r** is calculated from the projections in the plane ***MQN***, which is born from the projection of vector ***oP***. The segment ***oQ*** is the height of the vector ***oP*** in this coordinates. The angle **α** and **β** are the results of the tangent function from the projection **a** and projection **b** to segment ***oQ***. The angle ***γ*** will be explained later.

Table_1 Equations

$r = \sqrt{(a^2 + b^2)}$
$oQ = \sqrt{R^2 - r^2}$
$\alpha = \tan^{-1}(a/oQ)$
$\beta = \tan^{-1}(b/oQ)$
$\gamma = \sin^{-1}(a/R) \quad OR \quad \gamma = \sin^{-1}(b/R)$

The analysis of the spherical system opens the window for the inverse program to achieve a point on the spherical surface with the projected angles, which are gathered from the projected distance in the 2D coordinate. In this case, it is to gain the vector ***oP***

from the distance **a** and **b**. In the field of the 3D transformation and translation, the decomposition of rotation is one of the available solutions.

As shown in Figure 7, there are two ways to get the vector ***oP*** with the same effect. The first diagram shows the basic geometry relationship between the vector ***oP***, the projection plane ***QMN***, the projected line ***QP***, and the angle **α** and **β**. The problem is solved back forwardly. In the second graph, it shows the rotation order around the **x** axis and then the **y** axis. If the vector **oP** is the desired vector, which lies in the plane ***oPa*** constructing the angle **α** to the plane ***oP'Q'***, the vector ***oP'*** will become the transformed vector by the rotation of the plane ***oPa*** with the angle **α** around the axis ***ob*** or ***oY***. This is guaranteed by extending the segment ***oQ*** to ***oQ'*** to satisfy the length of ***oP'*** is equal to that of vector ***oP***, which makes the triangle ***oPa*** and ***oP'Q'*** congruent. Assuming the vector ***oZ*** sits in the axis ***oZ*** with the length of **R**, the vector ***oZ*** can be achieved by rotating the vector ***oP'*** with the angle ***γ*** around the axis ***oa*** or ***oX***. So the vector ***oP*** can be obtained by rotating the axis ***oZ*** around the x-axis with an angle ***γ***, then a rotation the vector ***oP'*** around the y-axis with an angle **α**.

Another way follows the rotation order from the y-axis to the x-axis to reach the same result as illustrated in the third graph of Figure 7.

Here, the angle **γ** can be calculated regarding the rotation sequence, as listed in Table_1 as well.

$$\gamma = \sin^{-1}(b/R) \quad OR \qquad \gamma = \sin^{-1}(a/R)$$

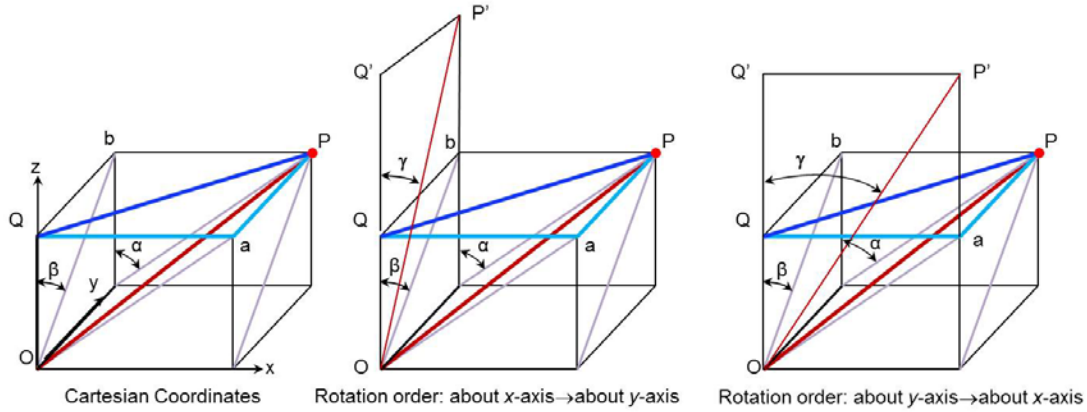

Figure 7: The Decomposition of the Rotation Transformation

By the preparation of the calculation of angles and the rotation decomposition, the final step of 3D rotation can be performed by the following equations (Table_2). The equation on the bottom row has two input parameters: the transformation matrix (either equation on the top row), and the initial 3D location corresponding to a zero shift pupil center.

Table 2 Three dimensional rotation

$$T = \underset{\gamma}{\begin{bmatrix} 1 & 0 & 0 \\ 0 & cos\gamma & -sin\gamma \\ 0 & sin\gamma & cos\gamma \end{bmatrix}} \underset{\beta}{\begin{bmatrix} cos\beta & 0 & sin\beta \\ 0 & 1 & 0 \\ sin\beta & 0 & cos\beta \end{bmatrix}} \quad \text{OR} \quad T = \underset{\gamma}{\begin{bmatrix} 1 & 0 & 0 \\ 0 & cos\gamma & -sin\gamma \\ 0 & sin\gamma & cos\gamma \end{bmatrix}} \underset{\alpha}{\begin{bmatrix} cos\alpha & 0 & sin\alpha \\ 0 & 1 & 0 \\ sin\alpha & 0 & cos\alpha \end{bmatrix}}$$

$$\begin{bmatrix} x' \\ y' \\ z' \end{bmatrix} = T \begin{bmatrix} x_0 \\ y_0 \\ z_0 \end{bmatrix}$$

From the above derivation, this algorithm is based on a rigid transformation and not limited to the spherical eyeball or tumor. The necessary input is the center location of interested target volume and the related 2D deviation from pupil center or the defined central position.

3.4 Alternative Implementation Method

As we have proven in Section 3.3, the tumor's position can be predicted from the pupil's position and a transformation matrix. Since the pupil on the sphere surface experiences the same rotations as the tumor, and the pupil's 2D coordinate is the projection of its sphere coordinate, this link can be expressed in the form of linear transformation. So a regression function based on linear model is adopted to look for the 2D/3D transformation matrix given the paired 2D/3D locations.

Considering the rigid relationship between the tumor and the eyeball (pupil) and a scaling/tilting factor between the image space and the CT space, combining above two linear systems, the tumor's coordinate can be related to the pupil's coordinate with the following relation:

$$\begin{bmatrix} X' \\ Y' \\ Z' \end{bmatrix}_{\text{Tumor}} = T \begin{bmatrix} X \\ Y \\ Z \end{bmatrix}_{\text{Tumor}} \text{ and } \begin{bmatrix} x' \\ y' \\ Z \end{bmatrix}_{\text{Pupil}} = T \begin{bmatrix} X \\ Y \\ Z \end{bmatrix}_{\text{Pupil}}$$

$$\begin{bmatrix} X \\ Y \\ Z \end{bmatrix}_{\text{Tumor}} = T_{2D/3D} \begin{bmatrix} x \\ y \end{bmatrix}_{\text{Pupil}} = \begin{bmatrix} T_{11} & T_{12} & T_{13} \\ T_{21} & T_{22} & T_{23} \\ T_{31} & T_{32} & T_{33} \end{bmatrix}_{2D/3D} \begin{bmatrix} x \\ y \\ 1 \end{bmatrix}_{\text{Pupil}}$$

The transformation T2D/3D can be established by linear regression through a set of corresponding 2D/3D coordinates.

This linear model function has already existed in the Matlab function lists, which is easy to pick up and could be served as a comparison analysis under certain conditions when the outcome from the innovated algorithm is not desirable. The name of the function is called GMLFIT, which is supposed to fit a generalized linear model using the input parameters. The result is a vector of coefficient estimates to become input

parameters for predicted vectors with the help of a function named GLMVAL. However, it might be a potential concern, when the console center is transferred to other programming languages. This is because it requires developing the linear model fitting algorithm from scratch, indicating far more time-consuming coding, testing and outcome comparisons have to be taken into account.

By analyzing the prerequisite parameters for this linear model, no specific requirements for the selection of the paired data set are necessary. This model works with the necessary calibration procedures, but does not strictly rely on it. The data sets from the five pupil positions are beneficial to find the desirable model in terms of the transformation matrix.

However, when the 2D/3D paired data sets come from exceptional circumstances, such as an unexpected rotation around the anterior-posterior axis, one 2D pupil position is mapped to multiple 3D tumor locations. If this happens, there exists a paradox in evaluating the outcome from the fitting function. If any satisfactory solution comes out of this approach, it is definitely a doubtful result. If no solution could be found, it makes it complicated to figure out the reasons for the odd inputs.

3.5 Calibration for Computer Simulation

This calibration is specified for the computer simulation and has no relation to the system calibration process. The transformation matrix is obtained from the geometric parameters based on a rigid spherical eyeball prototype. However, it is a better choice to build a software simulation to visualize the result. Therefore, the calibration between the computer pixel and the simulated eyeball phantom should be established first.

This idea creates the measurement of 2D distance between two pupil centers in the superior-inferior and the lateral-medial direction. At the same time, the projected 2D distance obtained from the 3D spherical coordinate can be calculated. Here, suppose the projected distance lies in the x-y plane, this distance only depends on X and Y coordinates and is independent of the Z value after the geometric derivation. Therefore, the calibrated result shows the ratio between the real distance from the simulated eyeball phantom in mm and the measured distance from the captured pictures in pixel along X and Y axis. Once the pupil center gets off the origin, the calibrated resolution will be helpful to transfer the distance from pixel to mm. Here, the resolution serves as the input for the calculation of the rotation angle as discussed in the previous section.

Specifically, the diameter of the eyeball is chosen as 32mm. This is a little bit larger than the averaged diameter of human eyes (around 23mm). The 3D eyeball is programmed to gaze at two end points on the horizontal line with 45 degree and the vertical line with 30 degree respectively. At the same time, four images were captured and the horizontal distance and the vertical distance in terms of pixels are measured. With the actual eyeball radius of 32mm, it is easy to calculate the horizontal and the vertical distance with different range of degrees. In this study, the ratio between pixels and distance of mm horizontally and vertically is achieved as 42.48 and 42.35, respectively, indicating around 42 pixels displayed on the interface are equivalent to one millimeter in terms of the unit of the computer simulated eyeball.

3.6 Simulation Application

This simulation is purely based on computer and programmed by Matlab, aiming to visualize the dynamic transformation between the 2D pupil center and the 3D eyeball.

Three image regions are allocated on the GUI, as shown in Figure 8. The left picture represents the 3D simulation with a transparent eyeball, a dark pupil and a solid tumor inside. The middle one mimics the pupil position inside an ellipse. The right one speaks for the synchronization of the dynamic pupil center inside an image gate from the tracking camera station.

The simulation could be performed under two conditions. First, the pupil center position comes from the user's choice by changing the pupil marker inside the second image region or from a file. The simulated eyeball phantom together with the accessories will update its view according to the geometric-based 2D/3D transformation algorithm. The tumor center location will be displayed on the frame. This procedure is helpful for the step to step confirmation during the beginning stage. The result becomes a dynamic simulation when a consecutive pupil position lists is loaded from a file. Alternatively, the pupil center position will follow the dynamic change from the tracking camera station simultaneously. The connection between the two computers depends on the serial communication. The pupil position will be updated at a sampling rate of 60 HZ, as well as the 3D simulation. This dynamic simulation will assist the system integration, the system test and the potential dosimetry validation via the CyberKnife.

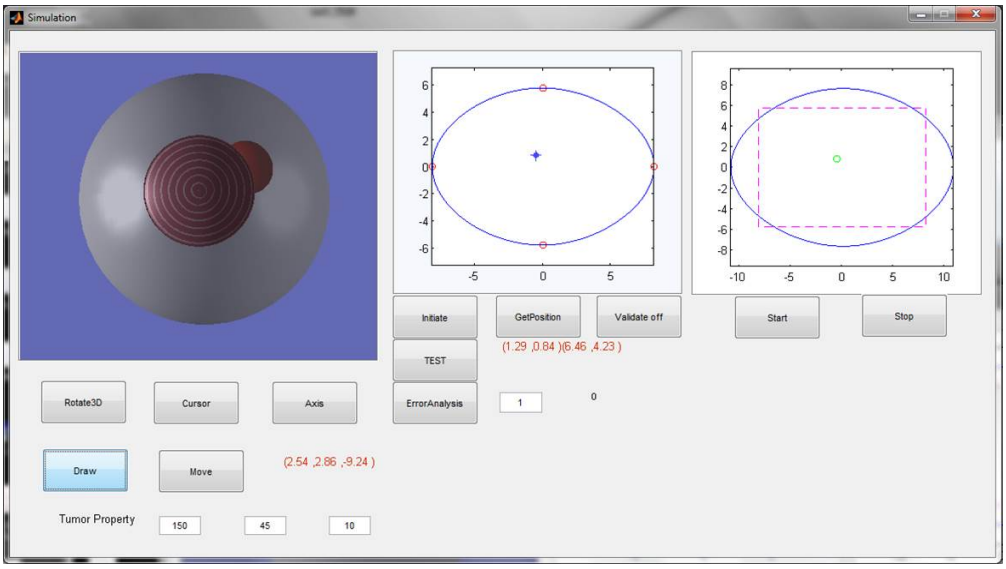

Figure 8: The Software Simulation Interface

3.7 Serial Communication

As introduced previously, we have a stand-alone workstation responsible for the eyeball simulation, the prediction of the tumor center and the linear stage driving. The exclusive camera software is located in another computer. Under this circumstance, serial communication becomes a practical connection between the camera station and the control workstation.

The pupil tracking camera package is commercially attainable, integrated with ISCAN boards and software. Both digital and analog signal output are available for a large amount of parameters, including the pupil center position, the corneal reflection position, the pupil area, the blink status, and the blink counter. This study was focused on the pupil horizontal and vertical center position. These parameters can be added into the output list on the tracking software.

The next step involves receiving the data and extracting them into digital format. Technically, digital signal demands an extra digital board for the system control computer, which calls for extra cost for this hardware and the condition of the computer.

Therefore, we choose the serial communication between computers, by which the pupil positions are delivered from com1 port in the pupil tracking computer, through a COM/USB transfer and eventually reaching the main computer via USB.

The independent communication software, named HyperTerminal, is employed to ensure the correct communication between these two computers. By triggering the output data flow from the tracking camera computer, the main computer can receive the selected parameters in text format. Users can compare the received data and the sent data displayed on two computers instantly to ensure the correct transport.

The coding of the serial communication is performed in Matlab after the initial confirmation by the HyperTerminal. It will be convenient to adopt a thread to deal with this data communication. However, it is unavailable for the later version of Matlab. Two alternative solutions have been attempted. One of them is a timer function that has a specific cycle time period to trigger the related functions for update status and graphs on the interface. This way is acceptable to a degree if the frequency is not higher than 10HZ. When the repeat time gets shorter, the graphic update is influenced and delayed, which is in part due to the inner execution of the Matlab environment. Another attempt, the current chosen method, relies only on the loop program. While the extracted signal satisfies the designated data structure or no stop command is issued, this model will keep on going. The benefit lies in no constraint on the data input frequency, either fast or slow input does not affect the performance of the function and has the serial communication solved.

Chapter 4 Mechanical Phantom System

4.1 Eyeball Phantom

Across the general introduction of the eyeball dimensions and eyeball movements in previous sections, the eyeball phantom can be simplified as a sphere with diameter of 32mm and made of plastic material to be compatible for CT or MRI scanning.

The phantom contains two hemispheres, which are connected by a pin-hole mechanism. Two holes are drilled on the edge of each hemisphere, and two pins are employed to lock the two half balls into one. In this way, the tight connection allows no relative rotations between the two half balls to ensure a clean rotation movement of the eyeball movement.

There is a cubic hollow space spared inside. It is reserved for deploying the tumor simulation material and the small metal beads as markers to simulate the tumor. The eyeball sphere and the metal beads are made by materials with different densities so that its 3D information by the CT scan can be identified easily. As shown in Figure 9, one plastic cube can fit in the hollow space. The cube is composed by pieces of shaped parts to carry the radiograph films when it comes to the irradiation validation. The solid cylinder inside at the off-set center is removable to reduce scattering during the validation test. In terms of the metal beads, the gravity center of these makers is extracted from the CT scanning DICOM file, and the averaged value serves as the simulated tumor center. Usually three beads are fine for reaching a 3D location.

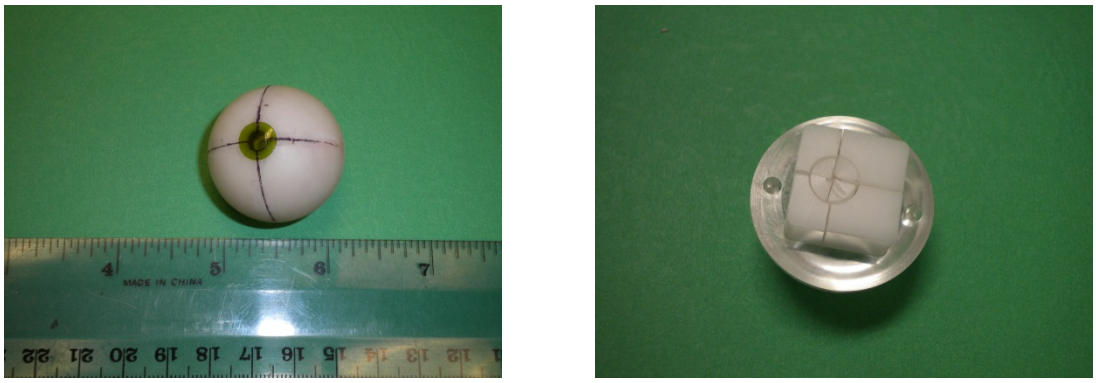

Figure 9: The Eyeball phantom module (Left) and the inside cubic square (Right)

On the surface, to absorb maximum infrared light emitted from the tracking camera and increase the image quality, an infrared absorber film (IA-film, ISCAN, Inc. Woburn, MA, USA) is employed for this purpose. The crossing lines are helpful for eyeball positioning in the manual way. Originally, the lines are finished by pencil drawing, which are reliable but easy to be erased. Then, one pair of crossing lines is etched by machine, which is supposed to be orthogonal.

4.2 Eyeball Holder

In physiology, human eyes sit inside the orbit, a spare space inside the upper front skull. For a simulation purpose, it requires a similar component playing the role of the orbit to allow eyeball rotations and eliminate translations inside a decent space. This function calls for the eyeball holder, which is responsible for keeping the plastic ball staying inside a limited space and only the rotation allowed.

This device contains two circular plastic plates, each with a circular hole in the center with diameter of 25mm, as shown in Figure 10. The bottom plate is transparent with a handle extending out to be attached to a solid column fixed on the frame bottom. The upper one is made of the same material as the eyeball module. The two plates are strengthened by four screws on four corners and are maintained on two parallel planes to

keep them co-centered. To assemble the plastic eyeball phantom and the holder together, the eyeball phantom is placed right on the center of the two plates. The upper pupil region is exposed through the open hole on the top plate, and the lower exposed eyeball is left for the connection to the extensible shaft.

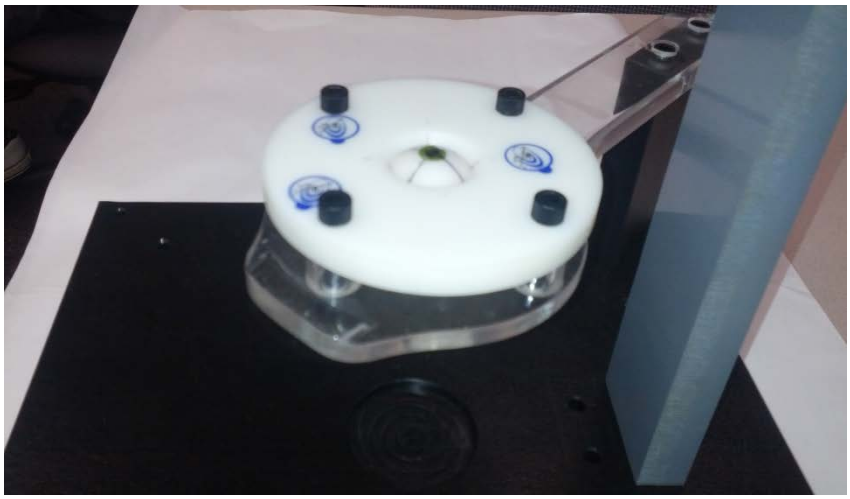

Figure 10: The Eyeball Holder

4.3 Extensible Module

How to convert the linear stage movement into the rotation of eyeball phantom becomes an important issue for the mechanical hardware. This connection has been attempted through several solutions.

The first module is based on the friction force between the eyeball and a soft rubber mat glued on the stage. When the stages are moving, the friction force gives rise to a rotation of the ball. However, the glue between the rubber mat and the stage surface became dry and lost the expected cohesive force, which results in an inhomogeneous flatness on the rubber surface. Another reason is the constant attaching between the plastic ball and the flat rubber results in a concave surface on the bottom layer, which

leads to a nonlinear rotation of the eyeball phantom when this concave region is driven towards or away from the center. This downside called for a new design.

To solve this problem, the extensible shaft is developed based on the bar model. As shown in Figure 11, L0 and L1 stand for the adjustable length of a shaft, D is the displacement of the linear stage. There exists a tangent relationship between the stage displacement and the origin length of the shaft. The angle between L0 and L1 covers the rotation of the eyeball provided no rotation on other axes. To keep the pupil inside the hole of the upper eyeball holder, and to maintain the steel stages within a region without artifact influences on the CT scanning, the evaluation of L0 and L1 can be obtained. This bar model is used to generate the dimensional parameters of the extensible shaft.

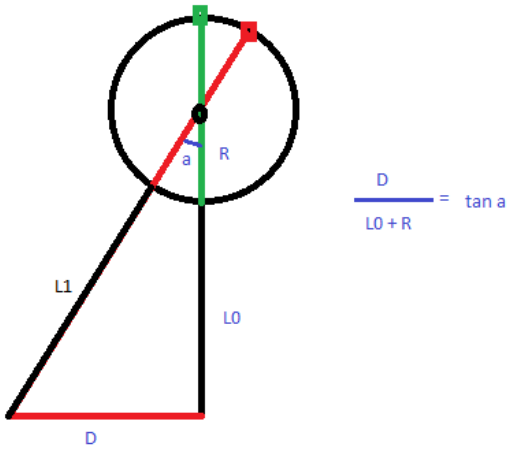

Figure 11: The Sketch of the Bar Model behind the Extensible Shaft

Regarding the extensible shaft, as shown in Figure 12, it includes a middle hollow cylinder, two pieces sliding rods inside the shell, one small sphere attaching to the stage and two screws at two ends of the rods to connect the eyeball and the small sphere. Specially, a small hole is drilled on each of the rods to constitute a pin-hole connection, which allows the pins sliding on their track and resulting in the changeable distance

between the two rods. For example, when the small sphere is dragged into a new position, the distance to the fixed eyeball will change by pushing the two rods together or pulling them away from each other.

In practice, the quality of manufacture plays a crucial role. Initially, the top rod was stuck at its initial position and only the bottom rod moved smoothly, which resulted in a half cutoff of the extensible range. To make the upper rod move as designed, a spring with an acceptable strength was inserted between the two rods inside the hull. This makes the two rods share the displacement evenly.

The assembled extensible shaft is integrated to the stage and the eyeball phantom. On the top of the stage, a plastic stack with a half-hemisphere concave at the center is to accommodate the smaller sphere on the bottom of the shaft. The linear movement of the stage will be transferred to a rotation of the eyeball phantom through the rotation of the smaller sphere and the extension between the two rods. The rotation of the eyeball phantom presents in a way of the movement of the pupil center, which will be extracted through the tracking camera.

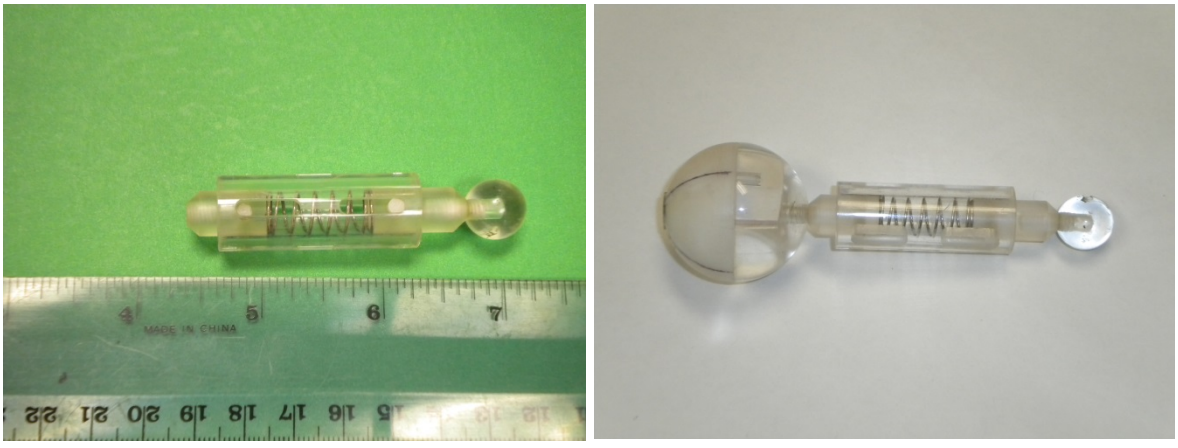

Figure 12: The Dissembled Extensive Shaft without eyeball (Left) and the Side View (Right)

4.4 Linear Stages

As earlier mentioned, the system is based on a simplified eyeball phantom, and the eyeball movements are only interpreted by two rotations except the anterior-posterior direction and translations. The simulation of eyeball movement could be fulfilled by employing two linear stages responsible for the driving force along the horizontal and the vertical axis so as to generate eyeball rotations around these directions.

The linear motion stage package (NSC-A2L) is commercially available (eTrack Low Cost Linear Stage, Newmark Systems, Inc. Rancho Santa Margarita, CA, USA). The specifications for the stepper driver are: 12-24 VDC, 1.5 Amp maximum current setting and maximum pulse input rate of 400K. The motor step of 133.333 steps/mm. The stage X is mounted on top of the stage Y, which connects to stage platform, where the extensible shaft sits. This package also includes the control software with an embedded programming function, allowing users the convenience to setup their specific driving modes, as shown in Figure 13. The two stages are programmed by a 2 axes stepper motor controller through the USB 2.0 communication as the requirement of mimicking different eyeball movement patterns. This assembled structure can be found on the system pictures.

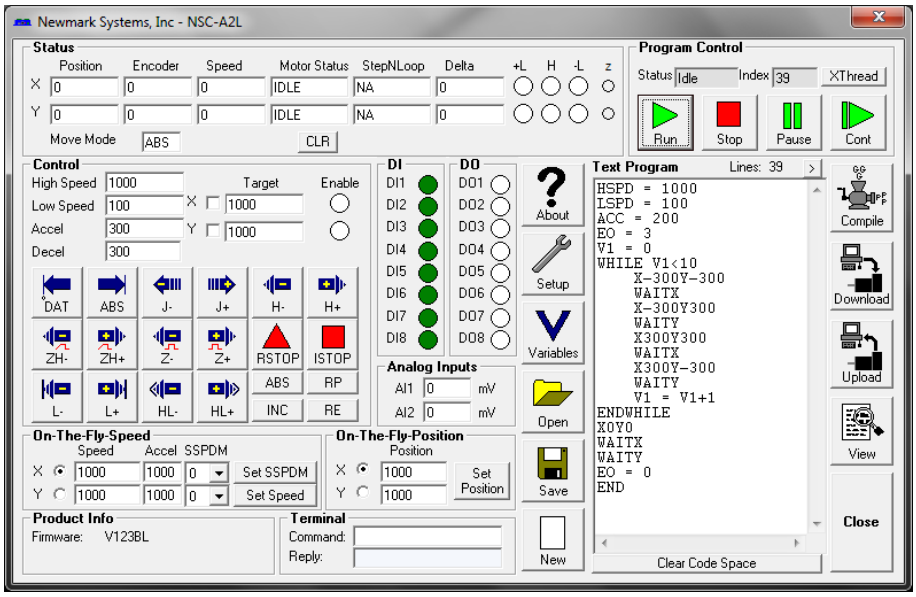

Figure 13: The Linear Stage Control Software with Editable Programming

Specific pupil positions and motion patterns were designed and programed for experiment demands. The pupil center coordinates are reflected in the tracking camera software when the eyeball phantom is driven to a specific position by the linear stages. The arbitrary positions can be finished by adjusting the displacement on the X and the Y stages. In this way, programmed patterns are generated by changing the position parameters, such as the reset movement, the left, right, up, and down, and an arbitrary positioning. The reset movement is designed to return the pupil back to the neutral status. The left and the right is a pair movement, which indicates the second move is finished after the first move with a reset movement. This design compensates and eliminates possible rotations during the pair movements to the maximum degree. Arbitrary positions are useful for the CyberKnife validation by assigning the arbitrary coordinates.

Different speeds are available for experiments. It shows the higher speed mode produces less noise with a speed around 5000 steps per second. The normal speed is chosen as 2000 steps per second for a quiet operation. Regarding the physiological

phenomenon of saccade, the peak angular speed is around 900^0/s for human beings, which is definitely out of the range of the linear stage. In this study, the exposed region in the eyeball phantom covers 102 degree, and 28.5mm in arc length. The saccade takes 0.11 second at a speed of 900 degree/second, and the linear stage has to spend 0.75 second at the maximum speed of 5000 steps/second. So the function of linear stage falls into the simulation of the regular eyeball movement at a relatively lower speed.

4.5 Tracking Camera

As introduced in the section for the eyeball immobilization, the tracking camera plays an important role for monitoring under a variety of clinical conditions, such as the proton therapy, the LINAC based stereotactic radiosurgery, and the CyberKnife. In our study, the tracking camera is assigned not only to fulfill the regular monitoring task, but also to extract the pupil features that are sent to the main control console instantly.

The commercially available tracking camera package (Model AA-ETL-101H, ISCAN, Inc. Woburn, MA, USA) is employed. It includes a tracking camera with infrared-imaging function, and a designated computer for live tracking, as shown in Figure 14. In terms of the hardware, the camera can work in the infrared mode, which ensures the imaging quality without influences from the environmental lighting conditions. The software offers the live monitoring and the display of extracted pupil features as customized. The data could be transferred to other computers or devices through an analog or a digital way. The software also provides a gated window to eliminate the occasions when the pupil goes out of the region. The interface looks like a steady opening eyelid surrounding the simulated pupil with a rectangle window. The extracted dynamic

pupil center coordinates are transferred to the console center with the serial communication through USB 2.0.

An assistanted camera holder is designed for two purposes: supporting and adjustment. The camera is embedded inside a cubic plastic shell, which is rigidly fixed on a plastic beam. The other end of the beam is sitting inside a horizontal hollow plastic slate. So the beam has a small range for the horizontal rotation to adjust the camera. Vertically, the slate is attached with two columns to change the height of the camera according to the distance between the camera and the eyeball phantom for the best image quality. When the tracked image quality is satisfied, the camera and the camera holder are fastened. In this way, the tracking camera and the phantom system can be kept in a relatively fixed position, which is necessary for the systematic validation and the error analysis.

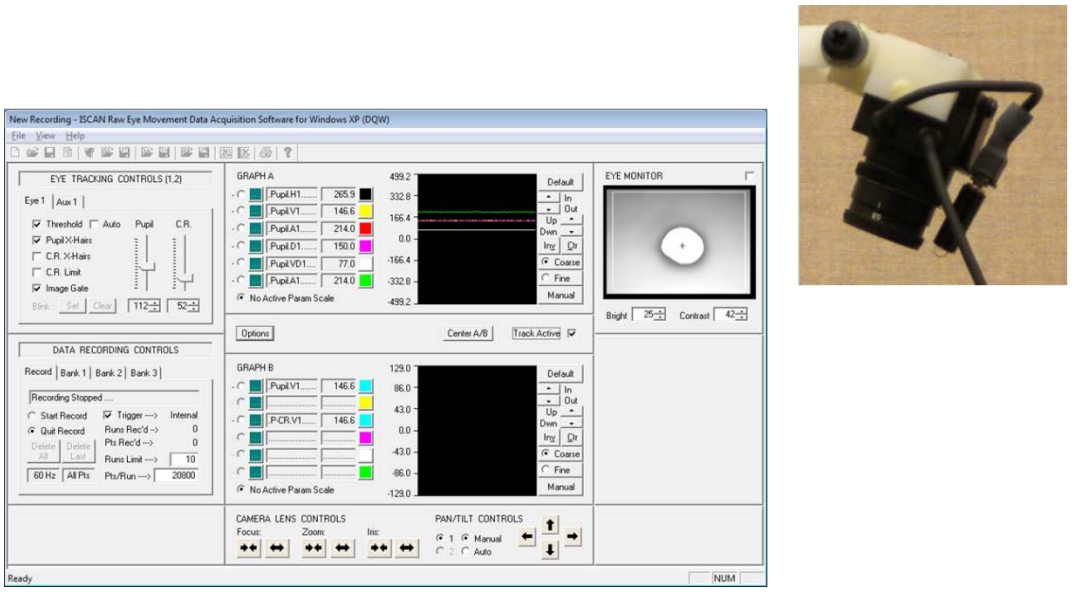

Figure 14: The Independent tracking software (Left) and the infrared tracking camera attached in the holder (Right)

4.6 Main Frame

The main frame supports each individual mechanical component and put them together as an integrated system. It includes a bottom platform, supporting columns, and connecting beams for some individual components. Several designs have been tried.

In the original version, except the square shape plastic platform and the supporting columns for the eyeball holder, the accessory for the camera holder was given three degrees of movement. The camera holder and the supporting column were connected by one single column between them. This connecting column could be rotated and leveled in order to adjust the camera position. However, this design lacked an essential requirement for the relative positioning of the camera and the stage, that the rotation angle between the coordinates of the camera image and linear stage was not desirable.

The second version chose a simple design with crossed beams paralleled to the linear stages, as shown in Figure 15 (Left). One thick beam with hollow center space is supported by two columns parallel to one axis of the linear stage. The other end of the camera holder is inserted into the hollow space of the first beam with a right angle. They are connected by plastic screws. In this way, the least height of supporting columns is achieved by the summation of the height of linear stages, the eyeball holder, and the camera-eyeball phantom distance. The camera holder can be adjusted in a smaller range for a better pupil positioning during experiments.

4.7 Assembled View of the Mechanical Phantom

Figure 15 shows a static picture of the assembled hardware components. The pupil is set at the center of the eyeball holder; the relative position of the camera is adjusted by changing the height and the horizontal position of the camera holder. As the pupil stays at

the neutral position, the extensible shaft endures the maximum tension, because the spring inside the shaft tube is suppressed to the shortest length.

Dynamically, the movement from the linear stages will be converted to the rotation of the small sphere ball at the bottom of the tube, leading to the extension of the spring accompanied with the rotation of the eyeball phantom inside the eyeball holder. This eyeball phantom movement simulates the clinical setting that the patient's head is fixed without any translation or rotation.

Figure 15: The Mechanical Phantom System (Left) and the Side view of eyeball phantom (Right)

Chapter 5 System Integration and Validation Design

5.1 System Integration and Performance

This section is elaborated for the system performance with the help of the detailed introduction of the optical tracking system and the mechanical phantom in chapter 3 and 4. The optical tracking system is nurtured by hardware and software. The software involves the general workflow, the derivation of a 2D/3D transformation algorithm, and the setup rule for the calibration both for the computer simulation and the validation process, and data communications. The mechanical phantom is composed by the essential phantom modules and the connecting frame structures as explained in Chapter 4.

In testing the systematic performance, the assembled mechanical hardware and the software will work together in sequence. First of all, it starts from the movement of the linear stage, which drives the eyeball phantom rotating inside the eyeball holder. Several programmed movement patterns are available for the stages. For instances, the stages can go in a square track, a zigzag line or a cross pattern. During the experiments, we found that the eyeball got stuck inside the eyeball holder when the spring inside the extensible shaft offered too strong forces. By considering the potential non-perfect force transformation between the eyeball phantom and the linear stages, the cross-driving pattern is chosen for the calibration and the reset operation before new movements.

At the same time, the pupil image is displayed on the tracking camera software in real time. The infrared camera holds the advantage of much less influences by the environmental light. Furthermore, an infrared absorption film is attached on the pupil region to strengthen the signal noise ratio under an infrared mode, as already shown in Section 4.1. Then pupil features, such as a pupil's coordinates, are extracted

automatically and sent to the console workstation through the serial communication with a frequency of 60HZ. The software provides options to setup a customized image window. When the point of interest jumps out the this specified window, the pupil center will become (0,0) as a default coordinates. This message will be picked up to control the radiation beams and suggest the patient to adjust the eyeball or have a rest.

The next step is defined as calibration and will be expanded in the following sections depicting the CT validation and the CyberKnife validation. In brief, the eyeball phantom is supposed to use at least five locations for the calibration, including the neutral position, the superior and the inferior position, and another pair of the lateral and the medial along the horizontal axis. The simulated tumor location is obtained through the CT scanning by averaging the gravity center of the steel fiducials inside the eyeball phantom. In this way, the pair of pupil position and the tumor location is obtained to calculate the resolution radio between the real distance in millimeter and that in pixel from the images. The neutral position could be used to find the real tumor location through an inverse transformation.

Eventually, the calibrated ratios along the two directions are saved. Together with the pupil center position, the related dynamic 3D tumor center location can be estimated by the 2D/3D transformation algorithm or the alternative functions. This tumor location will be uploaded to the CyberKnife system in real time so as to guide the movement of the robotic arm.

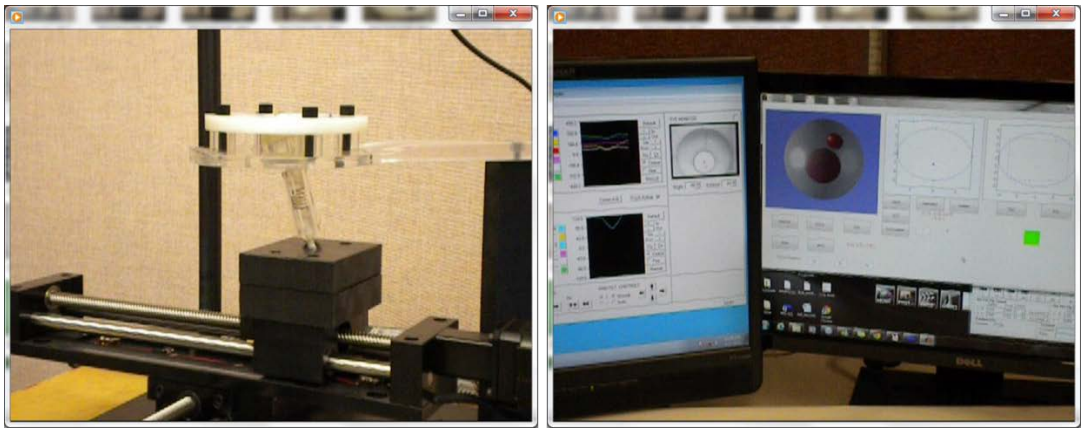

Figure 16: System Integration hardware part (Left) and software part (Right)

5.2 Validation of Transformation Algorithm

To ensure the functionality of the transformation algorithm from 2D to 3D, a validation method based purely on a computer graphic modeling is established. As a little touch of the software simulation in Section 3.5, one 3D simulated eyeball phantom with a tumor inside is generated. The eyeball phantom is set in a transparent mode so as to make the inside tumor "visible" for the observation purpose. An interactive process is developed to update the 3D eyeball phantom status by changing the 2D simulated pupil position via the mouse. Ultimately, it shows the workable transformation algorithm to calculate the 3D tumor location instantly with the alternation of the pupil position.

The validation is rendered as plotting the new tumor at the calculated 3D location and to see whether the original tumor can overlap with the new one. For easy observation, we chose different colors. The dark purple color is assigned to the original tumor, and the green color is used to cover the plotted new tumor, as simply shown in Figure 17. When the simulated pupil center is dragged to a new point, the eyeball phantom with the original tumor and the calculated tumor are updated accordingly. The result indicates the

good overlapping of the tumors and testifies the correctness of the transformation algorithm from the perspective of simulation.

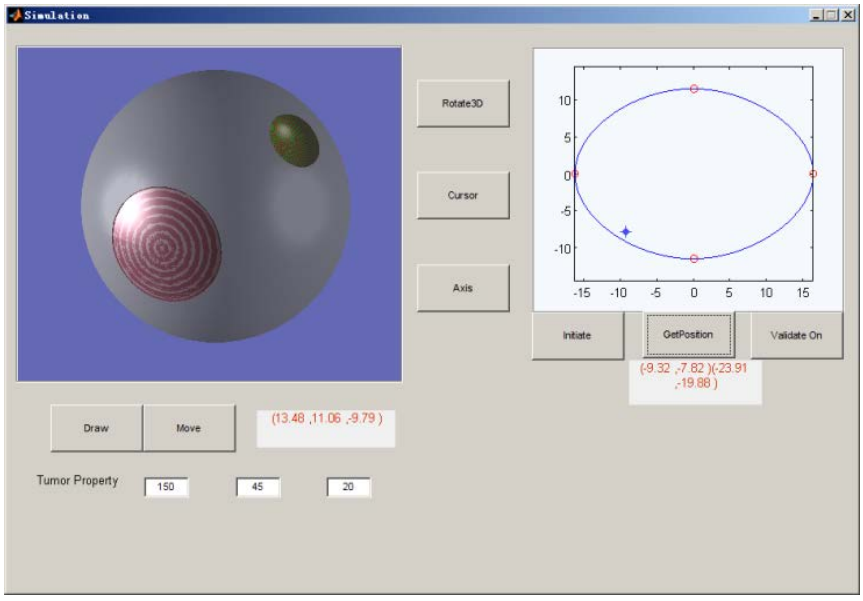

Figure 17: Validation of Transformation Algorithm by Software Simulation

5.3 Error Estimation

The error is associated with its components, either from the hardware or the software. Having confirmed the validity of the transformation algorithm, it comes to the evaluation of the performance of the hardware components in terms of this error.

First, the tracking camera application is responsible for both imaging and the image feature extraction. These functions are built-in already in the commercial product and are not practical to be changed from the programming level. One way for a desirable outcome is to adjust the related parameters, such as the setup options for manual or automatic recognition, the threshold for the pupil and the cornea reflection to find out the interested pupil region, as shown in Figure 18. The white region in the upper right image is the pupil region, and the cross hair marks the pupil center. The exact position is displayed in the center panel and the data flow ends up in the colored diagram beside the

live image. The other way is to ensure the image quality to magnify the pupil region signal and to eliminate the environmental noise. An infrared absorption film is adopted and attached on the plastic eyeball phantom serving as the pupil. In this way, the environmental noise in the CT simulation room and the CyberKnife treatment can be reduced to the minimum degree. At the same time, the difference between the images obtained under the two circumstances is reduced to the minimum degree as well. In this study, the flexible parameters for the pupil region recognition are fixed during all the experiments: 112 for the pupil threshold and 52 for the cornea reflection under all experiments. Another factor affecting imaging quality is ascribed to the distance between the object and the lens regarding the specific lens parameter of the camera. The camera should be well adjusted via the camera holder, where the camera is immobilized in, so as to achieve a high image quality and keep a relatively longer distance between the lens and the subject.

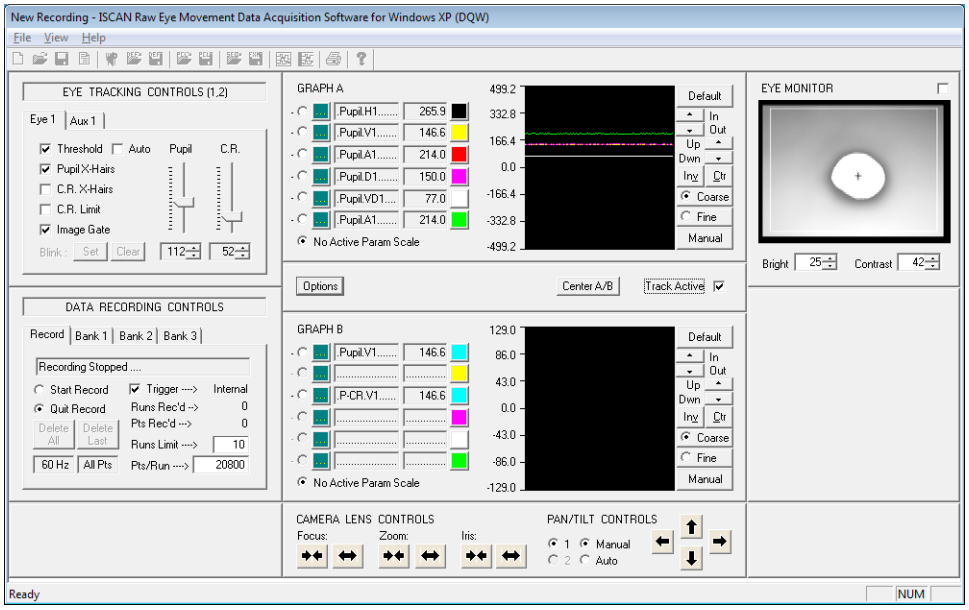

Figure 18: Tracking Camera Application

Secondly, the camera holder plays an important role to maintain a steady and clear imaging outcome. The first crucial factor comes with the height of the camera holder, which is determined by the adjustable lens of the tracking camera. In the original version, we tried a lens with 25mm and 16mm respectively. The 25mm lens brings a better focused image, but cannot cover the whole exposed eyeball phantom as desired. In the case of 16mm lens, it has to be put very close to the eyeball phantom to cover the whole eyeball image but ends up with a blurred image. After several rounds of communication with the camera company, we finally found a solution by utilizing a new 8mm lens to keep a proper distance between the camera and the eyeball, and obtain a clear infrared image. Eventually, the height of the camera is determined by the new camera lens. The second factor is associated with the fixation of the camera holder, which means the camera is required to stay steady. During experiments, we found the camera holder was rotated during transportation between experiment sites. It results in a rotated image, which will lead to an inconsistent recognition results. Several solutions have been attempted to fix the camera holder as displayed in the following systematic validation through the CT and the CyberKnife operation.

All of the above enumerated factors, from the camera lens, the camera holder, the movement transformation between the eyeball and the stages, will bring a combined offset to the pupil center. It is hard to obtain individual error weights from the systematic standing point. So a general error circle was employed to explain the systematic impact from this phantom system and the potential physiological factors from human eyes as well. This error circle could be used to predict the system error for any given radius, so as to serve as a guidance to retrieve and eliminate the potential dominate error sources.

The error circle is regarded to a circle with a certain radius according to the pupil center position to represent the range of an error. In this study, the listed error radius is 0.1mm, 05mm, 1mm, 2mm, 3mm, 4mm and 5mm, respectively. The analysis is looking for the averaged the 3D simulated tumor error distance based on one certain 2D error circle. In addition, the tumor location is taken into account for further analysis. In the 3D polar coordinates, three parameters determine a location: the radial distance, the zenith angle and the azimuth angle. The radial distance in this study is chosen as the radius of the sphere and will not be taken into as a factor. The only condition to pick up the radial distance happens when a translation movement shows up. The symmetric condition in a spherical phantom shows the azimuth angle has no impact on further analysis. The zenith angle is worthy to be taken as an impact factor. Therefore, only the zenith angle is selected and ranged from 0 to 180 degree with step angle of 30 degree.

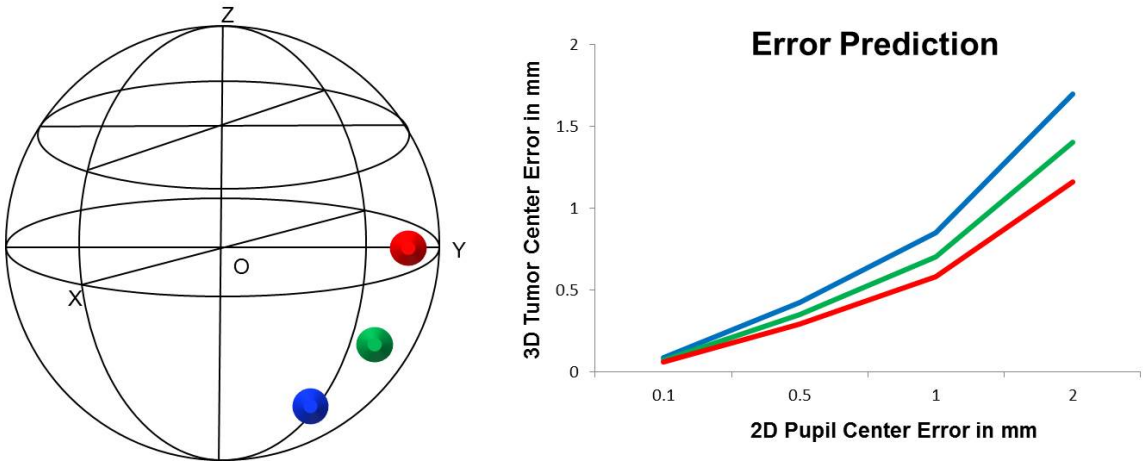

Figure 19: Systematic Error Analysis with Error Radius

As shown in Figure 19, we choose three of the zenith angles sitting under the horizontal plane as represents for the original tumor locations. They are assigned different colors in the figure. The error prediction result is drawn on the right. For the right diagram, the horizontal axis stands for a list error radius of 0.1, 05, 2, 3, 4, and 5mm.

The vertical axis tells the averaged 3D error displacement corresponding to each error circle.

This result shows the predicted error increases with the error radius in a nonlinear trend. But in the range 0.1 to 1mm, the lines approximately follow a linear trend. To obtain a system error under 1mm, the error radius for the pupil center has to be held under 1mm. Contributions to the error radius from different components of the system needs to be taken into consideration and balanced between them.

In terms of tumor initial location, the zenith angle of 0 has the lowest impact on the error prediction, the red color line as shown in the figure. The influence of zenith angle also follows a trend that the lower the error radius of the pupil center, the smaller error will be introduced. Theoretically, the zenith angle is unchangeable for a certain patient.

Based on the above analysis, we can conclude the error radius of the pupil center dominates among the factors for an error prediction. In this phantom, the contributive sources could come from the pupil center recognition, the nonlinear movement transformation, the unexpected eyeball phantom rotation, the location of tumor, etc. In the clinical condition, the patient and the treatment environment are potential triggers to increase the error radius of the pupil center. Detailed discussion is explained in the mechanical phantom components and Chapter 6.

5.4 CT Validation

The general workflow of this phantom system requires the calibration procedure to calculate the resolution ratio, which calls for the procedure of CT scanning. This is important not only to acquire the anatomic information for treatment planning, but also to

serve as a judge to determine the systematic quality with the error estimation. The slice thickness for CT scanning was 0.625mm. This process is split into several steps.

First, a few steel fiducials are glued to the inside wall of the plastic eyeball, as displayed in Figure 20. There were three fiducials in the early experiments and only one left before the latest phantom version due to the exchange of the bottom half plastic ball to apply the extensible shaft. In the last experiment, the fiducial markers were added up to three inside the cubic space. We have tried two types of beads with a diameter of 1.5mm and 3mm, since the experiments were taken in different hospitals. The 3D gravity center in the DICOM files will become the simulated tumor center. Another group of beads are attached on the eyeball holder and the camera holder to constitute the planes so that these 3D coordinates will be employed for the realignment under the CyberKnife system and for a better recognition of the noisy camera components.

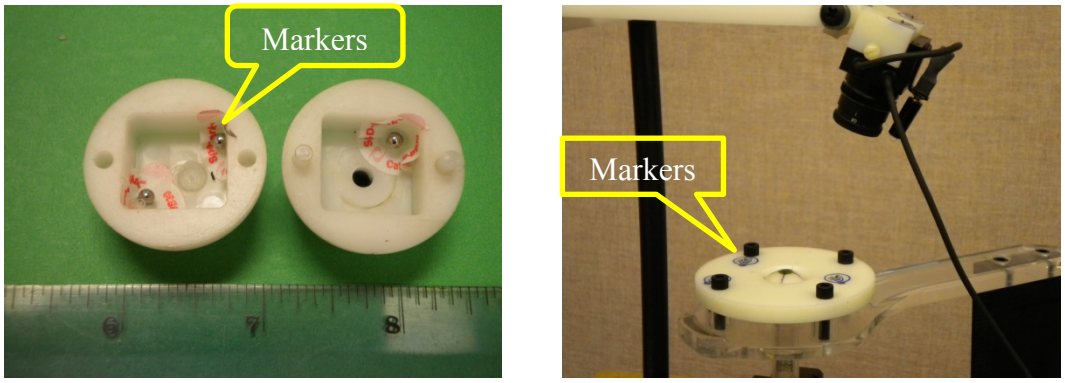

Figure 20: The Fiducial Markers inside the Eyeball (Left) and on the Surface of Eyeball Holder and Camera Holder (Right)

Second, there are specific setup requirements for this phantom system. As described in the section of camera holder, the height depends on the camera lens. At the same time, this height needs to compromise the conditions that the camera should not influence the imaging quality of the steel fiducials. Another issue comes with the fixation of the camera holder. We found the fact that the first camera holder rotated during the

transportation between the CT and the CyberKnife treatment room, see the left image in Figure 21. The ensued improvement adopted one rectangular column with a designed height regarding the requirement for the camera lens, as referenced in the middle image in Figure 21. The camera was screwed tightly, but the linear stages had to be clear away. The latest way falls back to the original fixation method by inserting the new screws on the other end of the camera holder to prevent the rotation of the beam, as shown on the right image in Figure 21.

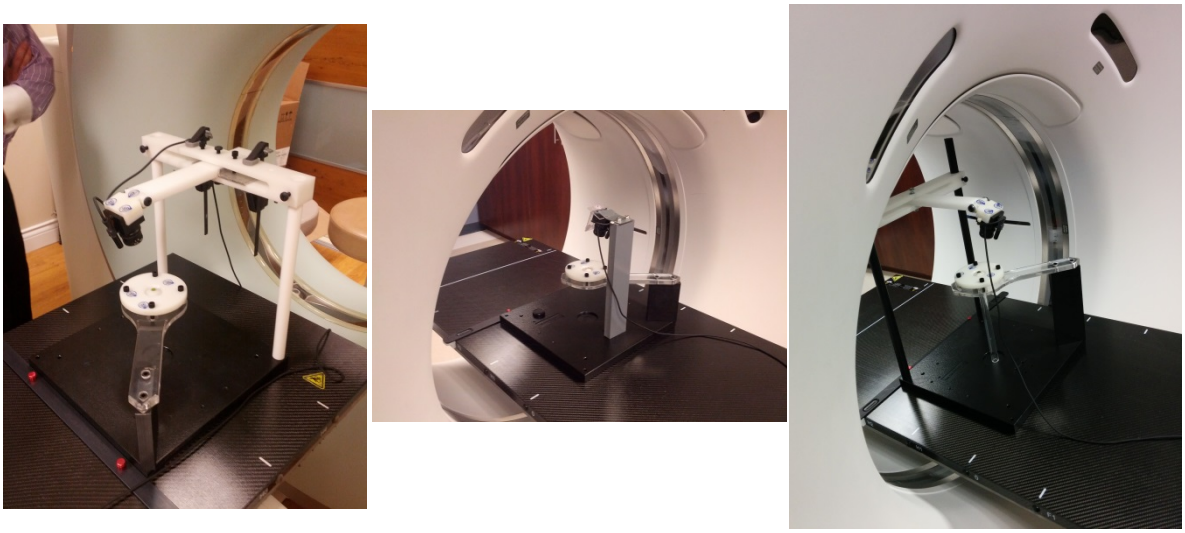

Figure 21: 1st version Setup for CT scan (Left), Improved version with a single upright beam (Middle), and the Latest Version with Tight Screws (Right).

Third, it is important to explain the workflow during the CT scan with the above equipped knowledge. The task of the CT scan offers the 3D information to calculate the resolution ratio between the millimeter and the image pixels. Four marginal plus one neutral pupil positions are the least requirements. The four marginal positions stands for the left, the right, the superior and the inferior pupil center locations required by the tracking camera software. The neutral position will be utilized to find the ground neutral tumor location by the inverse transformation. In the past experiments, all of the five pupil

positions are executed manually and adjusted regarding the live tracking images. It is performed manually because of the metal artifacts. Regarding the neutral pupil position, the eyeball will be setup to a position, where the extracted pupil center coordinate is close to the center of the image gate. In the case of the left and the right positioning, we try to keep the vertical coordinate for both positions consistent, and similar to keep the horizontal value the same for the superior and the inferior positions. The person responsible for the eyeball positioning will try not to introduce unexpected roation along the anterior-posterior axis. Eventually, the CT scan ends up with at least five pair of datasets with one 2D pupil center coordinate and one corresponding DICOM file to calculate and extract the 3D tumor location.

In particular, it is valuable to emphasize the manual positioning step for the latest system. As known already, the extensible shaft is employed to transfer the linear stage movements into the rotation of the plastic eyeball, and to support the eyeball phantom as described in Section 4.4. The linear motion stages cannot be mounted during the CT scanning due to the metal artifacts. However, they have to be installed during the CyberKnife tests. This condition will produce the inconsistent height of the eyeball phantom if no measures are taken to account for it. Here, we introduced a plastic tube compatible for the CT scanning to support the eyeball phantom and to maintain the same height when the motion stages are installed as shown in Figure 21 (Right). This height is measured and recorded by employing a precise gauge with precision of 1/100 inch. Under the CyberKnife environment, the linear motion stages are installed and repeats the previous height. This step plays an important role for the realignment between the CT DICOM data and the live CyberKnife images.

Thereafter, it comes up with the analysis approach for this validation procedure. As mentioned in the validation workflow, what we got are the pairs of 3D derived tumor center locations from the DICOM file and the 2D pupil centers from the tracking camera software. By utilizing the four margin data pairs, the calibration ratio between the millimeter and the pixel is obtained. By the inverse transformation, the tumor location corresponding to the ground truth neutral pupil center is calculated. These are the two prerequisites for the dynamic computation of the tumor location with pupil positioning. This operation has been introduced in Section 3.2. To evaluate the validation result, we defined an averaged error distance. The error distance is rendered as the 3D distance between the calculated tumor center and the acquired tumor center from CT scanning. Another metric is named as the root-sum-squared-error (RSSE), which comes from the root square of the averaged squared error distances. In comparison, the value from RSSE becomes bigger than the directly averaged result. For instance, the average of a data sequence from 1 to 9 is 5 and the RSSE is 5.62. In experiments, the extra data pairs except the five required ones are captured to bring a deep insight of the system performance.

Last but not least, another role of the CT scanning is to qualify the performance of the system with a phantom or a patient in clinical conditions. This relies on the estimated error distance of the tumor locations. If the error is out of the tolerance (1mm), something might be wrong and efforts should be taken to investigate the reasons. If the error is smaller than the threshold, the consequent treatment planning becomes feasible to execute.

Regarding the experiment setup, two separate outcomes measured by the geometric based the transformation implementation are listed in terms of the prototype and the latest version phantom system. The first validation came from our first CT scanning with the prototype components. This prototype stands for the setup of the pupil region and the cross-hair line to guide positioning manually. The pupil was drawn as a solid circle on top of the plastic eyeball by pencil as well as the cross-hair lines. These lines are put to prevent the extra eyeball rotation around the anterior-posterior axis. The downside of this way is apparent that the pencil drawing is easy to get blurred or erased accidentally. Thereafter, the cross-hair lines are etched by a professional mechanical machine and inked with a dark color. Another aspect change is the designed pupil as shown in Figure 9 (Left), that a round piece of infrared absorption film is attached on top of the plastic eyeball. Therefore, we have two groups of statistic results coming from the prototype and the latest phantom system, as listed in Table 3 and Table 4, respectively.

Table 3 CT scanning validation through prototype system

Pupil Position (Pixel)		Tumor center Location in DICOM (mm)			Calculated Tumor Center (mm)			Error Distance (mm)
x	y	X	Y	Z	X’	Y’	Z’	
264.6	112.2	-3.18	-206.12	179.60	-3.26	-206.01	179.31	0.32
260.7	186.7	-3.08	-207.53	181.46	-3.20	-207.42	181.10	0.39
255	83.2	-3.14	-205.57	178.20	-3.11	-205.72	178.47	0.32
369.1	117.4	-5.42	-206.08	179.50	-4.99	-206.06	179.40	0.43
153.8	109.8	-1.23	-206.74	179.20	-1.59	-206.62	179.29	0.39
187.4	78.5	-1.79	-206.15	178.31	-2.08	-206.01	178.40	0.34
365.3	188.6	-5.03	-207.64	181.58	-4.92	-207.56	181.24	0.36
256.6	110.4	-3.14	-206.02	179.26	-3.14	-206.02	179.26	0.01
Averaged Error Distance								0.32

Root of Summed Squared Error Distance (RSSED)	0.34
Standard Deviation	0.13

The calculated tumor centers come from the 2D/3D transformation as discussed in Section 3.3. The pupil positions are expressed in pixel and the tumor center location in the unit of millimeter, which are analyzed from the DICOM files. The calculated tumor centers hold the same unit in millimeter and are used to calculate the error distance based on the two 3D points. We can observe from Table 3 that eight data pairs are recorded and two statistics are obtained for evaluation. The error for the last data pair is close to zero. Because this position is used for inversion transformation and the predicted tumor location should be consistent with the original date, meaning the error distance should be kept close to zero. Here are averaged error distance and the root of summed squared error distance for assessment. Both of them are around 0.3mm and the standard deviation is 0.13mm. By ruling out the zero contribution for the neutral positioning, the averaged error distance and the standard deviation are 0.36mm and 0.04mm respectively. This outcome shows a promising outcome by positively confirming the successful performance of the prototype system and the calibration procedure.

Table 4 CT scanning validation through the latest phantom system

Pupil Position (Pixel)		Tumor Center Location in DICOM (mm)			Calculated Tumor Center (mm)			Error Distance (mm)
x	y	X	Y	Z	X’	Y’	Z’	
252.30	126.00	-11.70	-13.76	-5.16	-11.7	-13.76	-5.16	0.00
244.40	79.90	-11.63	-15.31	-6.95	-11.52	-14.60	-6.53	0.82
251.50	190.80	-11.83	-12.63	-2.02	-11.68	-12.80	-3.00	1.02
139.90	133.90	-8.50	-11.42	-4.65	-8.88	-11.73	-4.92	0.57
356.40	132.60	-13.81	-17.03	-4.96	-13.63	-16.10	-4.93	0.94
Averaged Error Distance								0.67

Root of Summed Squared Error Distance (RSSED)	0.76
Standard Deviation	0.41

Table 4 reflects the recent experiment based on the phantom system predicted by the geometric based the 2D/3D transformation algorithm. There are five necessary data sets, including the neutral position, the left, the right, the superior and the inferior positions. Similarly, the first dataset belongs to the recorded neutral position due to zero error distance value.

The averaged error distance for this experiment is around 0.67mm, still under our designed tolerance of 1mm. However, it is a little bit higher than the result from the prototype experiment. By reviewing the system error analysis, the predicted error shows a linear trend according to the error circle radius. So if an unexpected bigger estimated error is obtained, it means that some factors have resulted in a relative increase to the error circle and that people can make a root cause analysis to find the principle reason.

By combining Table 3 and Table 4, the error distance coming from the five calibration points are put together for paired t-test, and the obtained p-value is 0.05. Although, the two experiments were completed under similar, the statistic outcome shows the tendency that there exists a significant difference between the performances of the two systems. This test might become more persuasive if more paired data were gathered to show a significant different accomplishment between the prototype system and the latest system.

The tiny difference in the prototype system may account for the increase of the error radius and the inconsistency among the different data pairs. One consideration falls into the consideration of the etched cross-hair lines. These lines are important as references during positioning the plastic eyeball. The non-strict perpendicular condition makes it

easy to put the ball in a position with the satisfied acquired pupil center regarding the camera software, but the eyeball in fact has been rotated around the anterior-posterior axis. This situation could generate multiple tumor locations corresponding one captured pupil center. In this way, there will be a bigger error radius in terms of the pupil center, which eventually leads to a bigger estimated error distance with respect to the tumor location when compared with the predictions.

Regarding computation algorithm, we tried the alternative algorithm based on the linear model fitting. The following table shows that the calculated error in terms of the root-sum-squared-error is around 0.4mm [95], which is smaller than the outcome by the innovated 2D/3D transformation algorithm. This result shows a relatively even distribution of the predicted error for the tumor location center, which holds a lower standard deviation of 0.10mm compared with either 0.41mm from the 2D/3D algorithm.

Table 5 CT scanning validation through the latest phantom system via linear model

Pupil Position (pixel)		Tumor CT Data (mm)			Predicted Tumor CT Data (mm)			RSSE (mm)
P_x	P_y	T_X	T_Y	T_Z	T'_X	T'_Y	T'_Z	
252.30	126.00	-11.70	-13.76	-5.16	-11.58	-14.28	-5.05	0.55
244.40	79.90	-11.63	-15.31	-6.95	-11.37	-15.24	-7.10	0.31
251.50	190.80	-11.83	-12.63	-2.02	-11.57	-12.63	-2.15	0.29
139.90	133.90	-8.50	-11.42	-4.65	-8.82	-11.20	-4.56	0.40
356.40	132.60	-13.81	-17.03	-4.96	-14.13	-16.79	-4.88	0.41
Average RSSE (mm)								0.39
Standard Deviation RSSE (mm)								0.09
Mean Squared Error (mm)								0.40
Standard Deviation								0.10

Here, pupil's position identified by the video tracking camera is in unit of pixel in the image plane. Tumor's position acquired by CT scan is in unit of mm. The 2D/3D transformation produces predicted tumor's position in unit of mm. The root-sum-squared error (RSSE) is calculated by the following equation: $\mathrm{RSSE} = \sqrt{(\mathrm{T_X} - \mathrm{T'_X})^2 + (\mathrm{T_Y} - \mathrm{T'_Y})^2 + (\mathrm{T_Z} - \mathrm{T'_Z})^2}$. The mean-squared error (MSE) is calculated by the following equation: $\mathrm{MSE} = \sqrt{\frac{1}{5}\sum_{\mathrm{i}}^{5}(\mathrm{RSSE_i^2})}$.

5.5 CyberKnife Validation

Similar to the CT scan, a validation through the CyberKnife system requires a minimum five pair of datasets combing the pupil center coordinate and the recognized 3D tumor location under the CyberKnife system. It is the calibrated resolutions in this stage that are applied into the prediction of the new tumor locations as guidance for the CyberKnife. There are special specifications for this procedure.

First, this validation depends on the outcome from the CT scanning. Since the CT system and the CyberKnife system are two separate modalities, there has to exist a link to put them together so as to interpret the coordinates between them. This link is called the realignment. First of all, the therapist goes to the CyberKnife planning system to pull out the DICOM data and specify the regions of digitally reconstructed radiograph (DRR). The steel fiducial markers on the surface of the eyeball holder are circled automatically or manually, and similar way to achieve the eyeball center. Each of the markers inside the eyeball is marked and the averaged location serves as the tumor center. Next, the alignment occurs in the treatment software as the initial procedure before any treatment. The same eyeball position that is used to calculate the tumor center is reproduced in the CyberKnife treatment room. The live radiography images coming from the orthogonal

KV X-ray cameras are registered to the DRR images by adjusting the couch parameters with respect to certain thresholds. In our case, we chose the primary neutral position. After this procedure, the operation works in a way that the desired tumor center location can be acquired by only clicking the radiation button after one eyeball positioning manually or automatically by commanding the linear stages. The so-called tumor center location shows up in the form of a series of parameters for the couch corrections. This is because these parameters are relative to the origin; the new tumor location can be achieved by taking the opposite direction on the above variables. In this way, pairs of the 3D tumor center location and corresponding pupil position are recorded for further analysis.

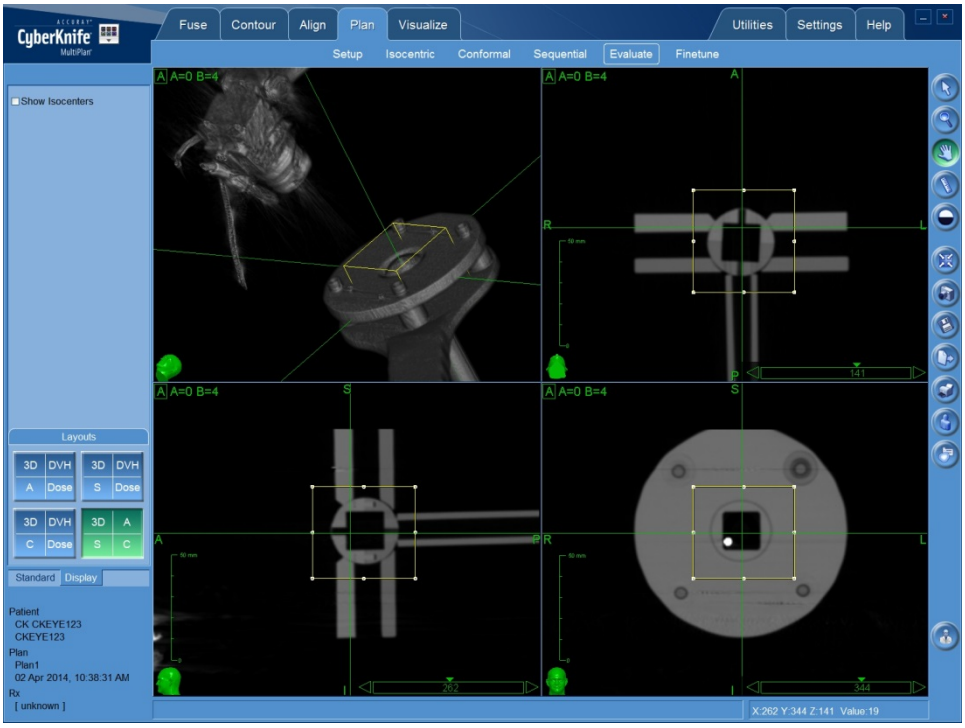

Figure 22: CyberKnife Plannig for Realignment

Second, similar to the requirement for the height of the camera holder appearing in the CT scanning, the height of the eyeball phantom becomes critical for the validation

under the CyberKnife system. Because the image guidance is based on the orthogonal radiation imaging technique, by which the x-ray goes 45 degree with the ground level to the subject from two sides. When the linear stages are installed and on the way of the projection, it might be difficult to pick up the fiducial markers inside the eyeball phantom due to the influence of metal artifacts. Taking this aspect into account, we took a deliberated calculation to insert a non-metal material block between the stage platform and the extensible eyeball shaft in order to eliminate the overlap, as shown in Figure 23. This calculation is based on the bar model as lay out in Figure 11. When the dynamic range of the pupil movement is defined, the displacement range for the linear stage is set. A 45 degree line is projected to reach the end of the linear stage at the same side of the projection (similar to distance D in Figure 11) for the deduction of the minimum height (like L0 in Figure 11), the summation of the eyeball radius, the height of the extensible shaft and that the inserted layer. This layer is chosen with 30mm in height.

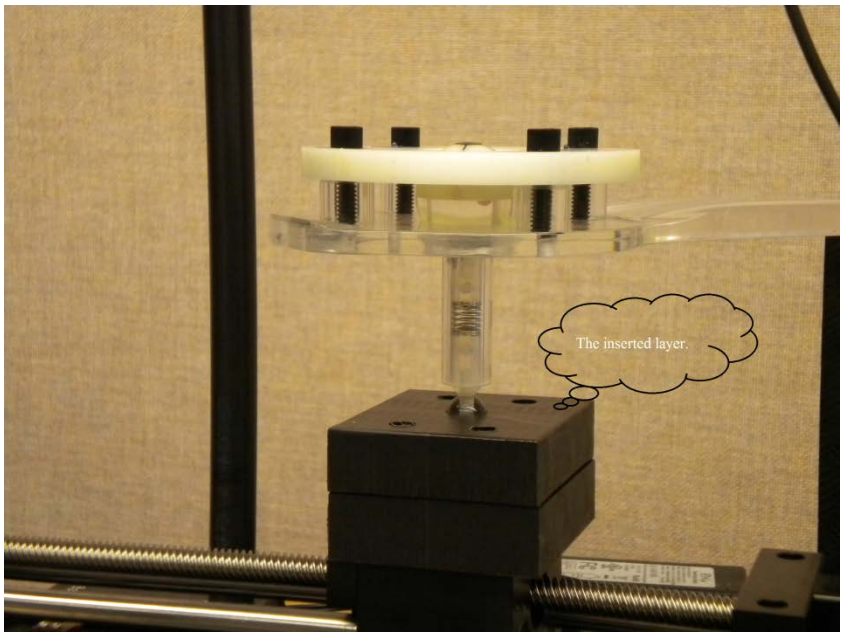

Figure 23: The Inserted Layer to Ensure the Height of the Eyball

Third, there is no upper limit for the number of the recorded data pairs. The least number could be one, the realignment position. In this way, the unit transfer from pixel to mm should base on the outcome from the CT calibration. Or to make another five positions calibration to obtain the resolution under the CyberKnife system. The difference from the CT scan is the instant response for the tumor location from the CyberKnife treatment software. This property makes it convenient to acquire more data pairs.

The appeared 3D tumor location indicated in Figure 24 as couch corrections under the CyberKnife system are transformed back to the CT coordinates with the help of the realignment parameters. At the same time, the calculated tumor location corresponding to each pupil position will compare with the recognized result from the CyberKnife.

Figure 24: Tumor Location from CyberKnife Treatment System

Next, this positioning procedure could be completed manually or automatically. For the CT scanning, it has to be done by manual since the installed stages will result in metal

artifacts. However, it is optional to choose the automatic way for the CyberKnife test, because the influence of the metal material could be avoided under certain circumstances, as long as metal parts stay in a tolerable distance from the steel markers and out of the 45-degree projection lines. In terms of automatic execution, each positioning of the eyeball phantom is managed after a reset operation to counteract any potential asymmetric mechanical movement. For instance, if the pupil stays at a left position, a reset operation to put the pupil back to the center is the initial movement before a second positioning. During experiments, we put the pupil at four corners (the up-left, the up-right, the lower-left and the lower-right) plus some arbitrary positions automatically.

Next, it is not a straightforward way to dig out the assessment feature for the validation under the CyberKnife System. Similar to the CT scanning analysis, we designed the averaged error distance in the CT domain as reference of the validation performance for the Cyberknife. But the result has to be transformed back to the CT domain. The first reason is the difference in both coordinate systems. The recorded DICOM file during the CT scanning follows the standard radiation image coordinate, which takes the positive direction on the right (axis x), the posterior (axis y) and the superior (axis z) respectively. However, the arranged corrected coordinate under the Cyberknife system picks the positive directions on the superior (axis X), the left (axis Y) and the posterior (axis Z) respectively. This inconsistency requires rearranging the order of each axis element for each input tumor center location under the CyberKnife system. As a result, the coordinate translation between the DICOM and the CyberKnife are indicated in the following equations, that $x = -Y$, $y = Z$, and $z = X$, here x, y, and z belong to the DICOM system and X, Y, and Z are the CyberKnife coordinates. Secondly, we

defined the eyeball center as the origin for the CT data after a linear translation, but the CyberKnife coordinate takes the tumor center as the origin. This demands another relative translation to put the comparison data coming from the same physical origin for both systems. So we recalculate the tumor location according to the eyeball center extracted from the CT data as the reference for the translation. After the order adjustment from the CyberKnife to the CT system and the relative translation, the tumor center in CyberKnife shows up in the CT coordinates. In parallel, the corresponding pupil positions are already fed into the 2D/3D transformation system to obtain the calculated tumor locations under the CT coordinate system. Therefore, the two groups of tumor location are put together to find out the 3D error distance, and series of 3D error distances are averaged to reach the eventual assessment for the validation under the CyberKnife system.

Last but not least, the evaluation of error distance will be influenced by the reproducible positioning of the mechanical components, such as the camera holder, the camera angle, the height of the eyeball, etc. For instance, if the camera holder beam was rotated due to transportation between places, it might be possible to find the same pupil center positioning as in the CT experiment, but at a compensation to change the camera angle. Eventually, it imposes a doubt about the camera image. It also raises questions for the realignment between the two systems, because the similar pupil center might map to a different tumor location by unexpected rotation of the ball during the neutral position repeat step. Next, when the estimated error from the CyberKnife system goes beyond the threshold, it is necessary to figure out the causes in the realignment procedure and the calibration steps. If the error is under the tolerance level, the calibrated resolutions can be

archived into a file and ready for the prediction of dynamic tumor locations with respect to those pupil centers.

For the latest version of the assembled system, we fulfilled an experiment on CyberKnife with 11 recorded pair data set of the pupil position and the tumor location. The estimated tumor locations were obtained through both the 2D/3D transformation algorithms respectively and are listed in the following tables. Table 6 shows the result coming from the geometric-based algorithm with an averaged error distance around 1mm and Table 7 illustrates the detailed results obtained from the linear model fitting function with averaged RSSE around 0.6mm. Both algorithms deliver an acceptable error tolerance, which is supposed to be around 1mm.

Table 6 CyberKnife experiment based on the latesd system via geometric-based algorithm

Pupil Position (Pixel)		Tumor Center Location in DICOM (mm)			Calculated Tumor Center (mm)			Error Distance (mm)
x	y	X	Y	Z	X’	Y’	Z’	
253.30	125.90	0.00	0.00	0.10	0	0	0.1	0.00
249.90	81.10	0.00	-1.30	-2.20	0.05	-1.024	-1.35	0.89
251.40	184.50	-0.20	1.10	3.20	0.03	0.93	2.26	0.98
162.30	130.80	2.50	2.00	0.40	1.60	1.32	0.24	1.13
341.10	130.40	-1.80	-2.20	0.10	-1.29	-1.37	0.28	0.99
173.50	89.70	2.00	1.10	-1.50	1.39	0.20	-1.33	1.09
316.90	93.10	-1.60	-2.90	-2.20	-0.96	-1.78	-0.78	1.91
339.40	184.30	-2.20	-0.90	2.30	-1.27	-0.47	1.95	1.08
161.50	184.90	2.00	2.90	4.00	1.62	2.13	2.60	1.64
324.20	184.40	-2.00	-0.70	2.40	-1.06	-0.21	2.01	1.13
178.60	90.00	1.80	0.40	-1.80	1.29	0.15	-1.30	0.75

Averaged Error Distance	1.05
Root of Summed Squared Error Distance (RSSED)	1.15
Standard Deviation	0.48

In Table 6, the standard deviation is 0.48mm, which is consistent with the value coming from the CT scanning predicted by the 2D/3D transformation algorithm for this latest system. By ruling out the neutral position dataset, the average error distance and the standard deviation becomes 1.15mm and 0.35mm. However, the standard deviation value still holds relatively higher.

This relatively bigger estimated error distance might be produced by the positioning strategy. Not like the manual positioning of the eyeball phantom in the CT scanning, the CyberKnife experiment utilized automatically eyeball positioning with the help of the linear stages. As discussed in Section 4.4, the eyeball is driven to the neutral position as reset operation before moving to a new position to reduce the influence of nonlinear movement transformation between the stage and the eyeball phantom. However, this standard deviation value even after eliminating the neutral position dataset is relatively bigger than the result coming from the CT scanning, which is executed manually. This difference indicates potential improvement might be needed to ensure the consistent movement transformation. In this experiment, few positioning operations didn't start from the neutral position, meaning the eyeball was not pushed back automatically by the linear stages as observed. Therefore, it is necessary to confirm the performance of the pupil center reset operation especially for the future irradiation validation, which requires the automatic operation without the presence of people due to radiation beams on the scene.

Table 7 CyberKnife experiment based on the lasted system via linear model

Pupil Position (pixel)		Tumor Cyberknife Data (mm)			Predicted Tumor Data (mm)			RSSE (mm)
P_x	P_y	T_X	T_Y	T_Z	T'_X	T'_Y	T'_Z	
253.30	125.90	0.00	0.00	0.10	0.10	-0.55	0.11	0.56
249.90	81.10	0.00	-1.30	-2.20	-0.20	-1.59	-1.90	0.47
251.40	184.50	-0.20	1.10	3.20	-0.31	0.97	2.73	0.59
162.30	130.80	2.50	2.00	0.40	2.33	1.91	0.43	0.20
341.10	130.40	-1.80	-2.20	0.10	-2.06	-2.69	0.20	0.56
173.50	89.70	2.00	1.10	-1.50	2.07	0.58	-1.42	0.53
316.90	93.10	-1.60	-2.90	-2.20	-1.45	-3.01	-1.44	0.78
339.40	184.30	-2.20	-0.90	2.30	-2.03	-1.29	2.62	0.53
161.50	184.90	2.00	2.90	4.00	2.34	3.29	2.85	1.26
324.20	184.40	-2.00	-0.70	2.40	-1.66	-0.90	2.64	0.46
178.60	90.00	1.80	0.40	-1.80	1.94	0.46	-1.41	0.42
Average RSSE (mm)								0.58
Standard Deviation RSSE (mm)								0.27
Mean Squared Error (mm)								0.63
Standard Deviation								0.26

Comparing with Table 6, the outcome shows a relatively stable prediction with a lower averaged error distance and standard deviation. It is due to the adoption of different estimation approaches. This fitting function has no strict requirements for the calibration procedure. However, the geometric based 2D/3D algorithm relies on the precisely calibrated pupil positions. In a way, the bigger error can raise more concern instantly, while the smaller estimated error might make problems ignorable, especially in this experiment with obvious observed undesirable performed reset operations automatically.

In another way, by applying the paired t-test analysis on the two set of error distance, the p-value is 0.004, indicating a significant difference between the two algorithms.

By comparing with the outcome from the CT scanning for the same latest system, the error and standard deviation (0.58mm and 0.26mm) are similarly bigger than values (0.39mm and 0.1mm) from the prototype system. In this way, it might reflect the same reason that the current automatic driving result is inferior to the manual operation. The cause for the relatively unreliable automatic positioning has to be the similar conclusion as the explained for Table 6. However, to make a fair comparison, the data from CyberKnife experiment is trimmed to the first five calibration positions. Therefore, the average error distance becomes 0.48mm, still bigger than 0.39mm - the value from CT experiment. This underscores the above conclusion that positioning methods lead to slightly different result, which might be the cause and should be improved especially during the irradiation CyberKnife experiment in the future.

Chapter 6 Discussion

This phantom system will be helpful to attain clinical trials dealing with the patients with ocular melanomas. In terms of the clinical trials, specific topics related to the physiological or pathetical circumstances will be taken into account, plus the performance comparison between the current results and the potential prediction in clinical.

6.1 Pupil Center Shift

As introduced in Section 1.1, there is a physiological phenomenon, named as pupil shifting [83, 95], in the presence of the accommodation and adaption under the influence of the environmental light intensity or specific drugs. The mean magnitude of the pupil shift could reach 0.15mm in maximum distance from mesopic to photopic and 0.2mm under the pharmacologic dilation. If this happens during treatment, it means the detected pupil center does not stand for the actually expected pupil center, and is affiliated with an offset deviation due to the environmental light changes or the pharmacological responses. According to the systematic error analysis, the pupil shift within a range of 0.2mm will introduce a corresponding error estimation of the tumor center by a value around 0.2mm. This will become a challenge when the tolerance is set around 1 mm.

In reality, the lighting intensity in the CyberKnife room is soft, comfortable and kept constant while patients are experiencing treatment. Another advantage for the CyberKnife radiosurgery is the non-invasive characteristic, so patients are not expected to receive pharmaceuticals related to the eyeball fixation. Or in another sense, the flexible measures could be adopted depending on the duration of the pharmacological effects. If it happens instantly or sustains for a short time slot, this situation could be avoided by

taking therapy after the specific time. If the pupil adaption can last for a longer time, it is recommended to reduce such prescription without impairing the patient's condition. Under such presumptions, although the pupil center shift might not be eliminated to a certain degree, it will impose little impacts on treatment.

On the other side, suppose the pupil center shift happens due to the accommodation in response to the environmental change, our systematic error analysis has taken care of this occurrence by predicting the error range of the tumor location according to the pupil center drift radius. As displayed in Figure 19, the introduced error depends on the shift range of the pupil center and the location of the ocular tumor. There exists an approximately linear relationship between the pupil deviation radius and the resulted error for the tumor location. The bigger estimated error indicates larger pupil deviation. Therefore, we could define a tolerance pupil deviation radius, which can be reflected during the error analysis for the CT scanning. If the calculated error distance is above the tolerance, it is critical to figure out the dominant reasons, such as the unstable lighting environment, patient's anxiety or related drug factors, and take corresponding measures to reduce the pupil deviation radius as much as possible. When the predicted error for the CT scanning is within the tolerant level, the consecutive treatment will become feasible.

6.2 Eyeball Movement

Eyeball movement is generally classified into voluntary and involuntary movement during the performance of the fixation or the tracking upon the external stimulus. Regarding fixation, it refers to the vestibule-ocular reflex (VOR) and the optokinetic reflex and the gazing-shifing mechanisms in terms of saccades and pursuit movements. In the case of the fixated head, saccades do not generate rotations around the anterior-

posterior axis under the Listing's Law. The velocity of a saccade linearly depends on the angular distance the eye travels during the movement. If the amplitude is over 20 degree, the head rotation is involved. When the head gets fixed, the maximum velocity stays around 400 degree/s according to the linear relationship, given 300 degree/s for 10 degree and 500 degree/s for 30 degree.

Our study was taken under a situation that the head is fixed. The concern is the involuntary high speed gaze-shifting during the treatment provided the patient's head is fixed decently. In reality, the triggers having influence on the potential involuntary eyeball movement will be limited to the maximum degree. The treatment room is set up with comfortable light environment, which might be helpful to exclude the chances for saccades. At the same time, we chose the signal sampling frequency with 60HZ in the tracking camera, which increases the tracking capability to obtain the instant pupil position. The last but not least, an adjustable image-gate is brought up in the tracking software in case the recognized pupil center wandering out of the specific region due to the voluntary or involuntary eyeball movements. In a sense, the image-gate plays a role to filter the wild excursion in order to reduce the frequency to report the pupil center positions.

Given these efforts to catch the live pupil position, there is still a question lying behind the technique of the treatment by the CyberKnife. In general, it might take around 30 minutes to fulfill one fraction, which will bring more chances for the involuntary eyeball movements and/or saccades in the later section after a relative long time gazing. Hopefully such kind of problems could be compromised during treatment planning stage

by professionals. For example, it might be possible to insert some time intervals for patients to have a rest, and then continue the treatment.

6.3 Blinking

Blinking happens all the time when the eye is open, takes typically around 0.1 to 0.2 second. It is not an easy phenomenon to simulate. It deals with both the time dimension and the eyeball spatial domain. Regarding time dimension, the blinking duration, the frequency, the incidence distribution and the direct causes are essential factors to be taken into consideration. In terms of the spatial domain, the status of the eyeball before and after the incidence of blinking raises a question, that the transition and/or rotation of the eyeball might be induced but without notice. Literature study shows eyeball rotation happens during the blinking, with a minimal occurrence for the initial straight-ahead gaze and other cases smaller than 5 degrees. The rotation period is around 50 mSecond. However, the impact of the eye ball retraction draws more attention by introducing 1 to 2 mm of eye globe backing into the orbit [85].

In contrast to the impact of the pupil shift due to the accommodation and adaptation, the backward translation along the anterior-posterior axis introduces much more troubles. The foundation of our transformation algorithm is based on a rigid model with limited rotations and without presumed translation as the head gets fixed during treatment. If the risk factor of translation is taken into account, the displacement of the translation along the anterior-posterior axis will produce the same amount of predicted errors by obeying the rigid model. This can only be caught when the upper eyelid returns to open, and the approximate orbit translation should stay under 1 to 2mm before the blinking phenomenon finished. This type translation also brings an odd scenario that the tracking

camera may lack the capability to distinguish it from normal conditions when the eyelid restores to the open state. In addition, the rotations, except along anterior-posterior axis, are estimable based on the systematic error analysis, and reflects in the shift of pupil center.

Considering the impact of blinking, potential approaches might be available for further study. First, a certain device to simulate the blinking-introduced translation is helpful to investigate the actual influence of blinking during the radiosurgery treatment. Further models could be developed to generate a blinking window and an adjustable blinking frequency so as to pick up the valid pupil information with limited impacts from blinking. Another help may come from the blinking options on the tracking camera. Currently, some data have been recorded regarding the blinking setup with 80% coverage and the no blinking condition upon a steady pupil. The data distribution shows no big difference between the two dataset. By adopting the blinking function from the camera and the potential blinking models, it will be possible to find an answer for this issue.

6.4 Effect of Camera Angle

Technically, the camera is supposed to be set up parallel to the subject in order to obtain a rigid image. If there is an angle (e.g. 45^0) between the plane of the lens and the subject, it has to take an affine factor into account during the calibration and correction for every recognized pupil center from the software. There is one exception to ignore the affined imaging effect, when the distance between the lens and the subject are considerably further enough from the subject or the subject presents in a smaller region.

In reality, the camera angle is an unavoidable issue. The camera is not allowed to be laid on top of the eyeball phantom to keep them in parallel planes. It is because the

camera and the subject will take CT scanning at the same time, and bring metal artifacts. They will make it hard or impossible to recognize the implanted fiducials inside the eyeball phantom. Therefore, a certain angle will happen between these two planes.

Apparently, as the increase of the camera angle, the vertical resolution will grow in terms of mm/pixel, while the horizontal value might have little change. For instance, if the camera is kept parallel to the imaging object, the two resolutions should be identical. When the angle increases, such as 45 degree, the resolution difference will obviously be increased.

In our first CT scan experiment, the camera angle was around 15 degree by extending the camera beam. The distance between the lens and the eyeball phantom is around 70mm. The pupil center was drawn manually in the form of a solid circle with a radius around 3mm. At the same time, two resolutions along the orthogonal coordinate in the image plane are calibrated to compensate the influence of the imaging angle. The eventual averaged error distance is 0.32mm. This shows that a certain camera angle could be allowable if the distance is relatively far between the lens and the subject, and the interested subject is comparatively smaller.

To obtain a comprehensive investigation, the clinical application should pay attention to balance the tilted camera angle and the distance between the camera and the patient. If condition doesn't allow, it has to work on the analysis of the affined resolution.

6.5 Mark Lines on Eyeball Phantom

The marked cross lines on the eyeball phantom delivers an easy check to identify the unexpected rotation around the anterior-posterior axis. Under normal circumstances, these lines are supposed to stay parallel to the cross lines etched on the eyeball holder. No

matter how this eyeball phantom is placed or driven to a location manually or automatically, more attention should be paid if the parallel situation is interrupted. This indicates an ambiguous situation of a rotation around the anterior-posterior axis. Then the calculated tumor location according to the skewed pupil center doesn't reflect the real tumor location, and introduces certain errors.

Regarding the accumulated experience from experiments, it shows the function of the crossing lines. In the first CT experiments, those lines on the eyeball phantom are drawn by hand and strictly perpendicular. The error was hold as 0.45mm in maximum, which is a promising outcome. In the later experiments, some changes have been done to the eyeball phantom. The pupil region was drilled as a circular hole, which makes it difficult to recover the original markers. Therefore, those cross lines were etched on a mechanical machine and ended up with the unexpected non-strictly paralleled marker lines. Then the outcome from the similar CT experiments procedures ended up with an error around 0.7mm.

The crossing lines are helpful during the phantom stage, but cannot be mirrored to the clinical treatment. It is not necessary to worry about it. Because the function of the cross lines in the phantom system is to help reduce the happening of the unexpected rotations. While in real treatment procedures, the patient and the head are fixed on the couch respectively. Especially the head is left no freedom for any movement, which eliminates the unexpected eyeball rotation around the anterior-posterior axis by vestibule-ocular reflex (VOR) due to the movement of head.

6.6 Comparison of Transformation Algorithms

We have developed a geometric-based 2D/3D transformation algorithm assuming the eyeball is taken as a rigid system. The first outcome from the CT experiment showed the estimated error distance is under 0.45mm and the averaged error is 0.32mm. As the project is progressing, another linear model based fitting function was adopted, which is a function in Matlab and easy to use. Therefore, the prediction results for both the CT and the CyberKnife experiments are listed in Section 5.4 and 5.5. We can see the results are encouraging and within the acceptable tolerance (1mm) for either algorithm in terms of the CT experiments. The average error is 0.39mm for linear model based Matlab function and 0.67mm for the 2D/3D transformation algorithm. Similar scenario happens for the CyberKnife experiment with an averaged error distance of 0.58mm and 1.05mm, respectively. Especially a paired t-test obtains a p-value of 0.004, indicating a significant difference between the two algorithms for predicting the systematic error. Both of them have their pros and cons, and it is not appropriate to make a conclusion during current stage.

First, the execution of the geometric-based 2D/3D transformation algorithm is efficient and easy to transfer to other programming environments even though programmed with Matlab, because this performance doesn't include any complicated sub-functions embedded in Matlab. However, the linear model fitting has layers of sub-functions. This requires much more efforts to interpret the Matlab function into other programming languages and it might not be that easy to realize the bottom sub-function in another platform due to the potential limited mathematical libraries.

Second, the Matlab function has the advantage of easy to use, taking comprehensive variables into account and convenient to change parameters, such as the type of linear model. However, the geometric-based algorithm only relies on the input data pairs and necessary variables for calculation, such as the extracted ball center from the 3D DICOM data.

Next, theoretically, the fitting approach doesn't require a strict calibration procedure if only each data pair is unique. For example, the pupil margin position could be offset to the virtual horizontal or vertical axis, which maybe a frequent phenomenon happening in the clinical condition. Besides, the number of data pair is not limited to a certain number. However, the geometric based algorithm needs at least 5 data pair to complete the calibration procedure.

Last but not least, the original geometric-based algorithm demonstrates its sensitivity to the experiment setups, while the fitting function shows a high tolerance to abnormal occasions. For instance, in the cases of the CyberKnife experiment with the latest system setup, the predicted errors are approximately 1.1mm and 0.6mm for the derived algorithm and the Matlab function, respectively. There was an issue to reset the pupil during the automatic calibration process, and it was observed. The outcome from the derived algorithm reflects that something abnormal happens due to the bigger predicted error distance. This is a helpful alarm to analyze the cause of the problem. While judging from the number, the Matlab function implies the better performance in predicting but ignored the implicit problem. Therefore, the derived algorithm might be a candidate method to test the performance of the system due to its sensitivity, and the fitting function could be taken as a predictor during radiation surgery to reduce the estimated error.

In summary, both approaches have their capability to predict the tumor location depending on the pupil center coordinates. The complex clinical conditions will sift the more robust and sensitive one as the final choice, or take both of them at different operation stages.

6.7 Clinical Envision

This whole phantom system initiates from the idea to offer real time guidance for the CyberKnife to apply the radiosurgery for uveal melanomas or ocular tumors. The advantage of this application presents in pinpointing the tumor center precisely and noninvasively, and reducing the irradiation to the surrounding normal tissues. Patients will benefit from the accurate image-guided radiosurgery by the CyberKnife without invasive surgery and pains. However, this guaranteed solid outcome from phantom system might face challenges in clinical conditions, when the patient's eyeball replaces the phantom eyeball. More considerations should be taken into account to ensure a successful transition.

First, mechanical components might be called for new arrangements. The dimension of the main frame is subjective to hold the patient's head in order to put the tracking camera right on the patient's eye with certain distance. For one specific lens in the tracking camera, the distance between the camera and the patient's eye should be kept in a limited range to achieve a clear image. In other words, if the distance cannot satisfy this condition, the lens will have to change. From the perspective of systematic reproducibility, the adoption of certain precise components will benefit clinical operation, such as a meter to show the tilted angle of the camera, the horizontal displacement of the camera holder, the readout of the eyeball phantom height during dosimetry validation, etc.

Second, the validity of the extracted pupil position might incur doubts. When the real patient's affected eye replaces the eyeball phantom, it will become a complex situation. Taking the iris melanoma, the extracted pupil position will be influenced by the irregular expansion of the tumor area into the regular pupil region. Can the software automatically recognize the right pupil center? If the pupil region holds its integrity, it is up to the patient's performance of gazing at neutral position. The concern is the tracked eye is the affected eye, which is not assumed to work effectively due to the pain or other uncomfortableness. In addition, the patient's eyeball can't be fully exposed to the same size as that of the phantom eyeball. This requires the same accurate pupil recognition for the partially exposed eyeball. Although this feature has been considered in the tracking camera software, it still needs sufficient clinical examples to show the effectiveness.

Third, the calibration procedure needs to accommodate the inaccurate positioning. In clinical setting, it is hard to draw the crossing mark lines on the eyeball to ensure the marginal positions constitute strictly perpendicular lines. However, extra efforts are possible to guide the patients to focus the diseased eye to certain position. For instance, a specific light source is feasible to float on a track composed of two perpendicular lines. In this way, the virtual crossing lines will complete the function of the mark lines on the phantom eyeball.

Fourth, the gazing status during treatment is another concern. In literature, some studies utilize a fixed light source to help patients gazing and focused at one point during the treatment. However, it may present different results due to different input parameters, such as the intensity, the dimension or the position of the light source. Another concern is about the different light intensity to the background. It is potential to introduce the pupil

shift after losing focus due to the involuntary movement. Alternatively, it is possible to finish the treatment without the help of the light source guidance. Patients are told to focus on the radiation tube at their comfortableness, where the background is consistent with that of the treatment room. In this way, the phenomenon of pupil shift might be ruled out.

Fifth, further investigation on the tracking camera is helpful in terms of picking up the related 2D information from the normal and the abnormal eye. For instance, the blinking analysis could be implemented regarding the patient's eye, so as to find the accurate relationship between the blinking and the predicted errors. Furthermore, some noninvasive measures might become practical to reduce the happening of blinking according to literature studies.

Sixth, the psychological status of patients will contribute to the pupil accommodation and introduce affiliated pupil center shift. For instance, the influences imposed by the background noise, such as the treatment machine noise and the background music, could make patients feel uncomfortable and result in pupil change. Similarly, the patient's fear, anxiety and excited feeling could bring similar results. This suggests specific earplugs to block the noise and necessary communication are essential to reduce such influnces.

Last but not least, certain clinical assessment in terms of the objective features and the survey will be helpful to confirm the treatment effect by the CyberKnife. The objective features could include the test of vision acuity for the affected eye before and after the treatment. The survey reflects the subjective response from patients and is a vehicle to collect the potential treatment complications, the effectiveness to the tumor control and the recovery situation during the follow-up period.

Chapter 7 Conclusion

Since the traditional radiosurgery is accompanied with the invasive surgery procedure and has limited degrees of freedom of movement for the radiation beam delivery arm, our study proposed to establish a solution to the noninvasive treatment of uveal melanoma by the CyberKnife. It is characterized by an eyeball phantom system and an estimation of the tumor center in real time.

We built a mechanical eyeball phantom system driven by the linear motion stages and monitored by the infrared camera. The eyeball phantom is made of CT/MRI compatible material. The specifically designed extensible eyeball shaft becomes a buffer to drive the rotation of the eyeball phantom. Different versions of main frames and the camera holder have been attempted during experiments. The system is eventually integrated and validated through the CT and the Cyberknife environment.

In terms of the real time tumor localization, we derived the intrinsic rigid geometric relationship between the eyeball and the tumor. A 2D/3D transformation algorithm is developed to estimate the tumor location from the pupil center. Based on the 2D/3D transformation, a linear regression function was implemented as well. Both ways were validated with the CT data and under the CyberKnife system. Outcomes of the validation are satisfying and promising.

The potential coorperation between the CyberKnife company will offer the opportunity for the radiation validation by CyberKnife. When it meets acceptable error tolerance, the future clinical trial will be applied.

In terms of my contribution to this dissertation, it includes the derivation of the 2D/3D transformation algorithm to predict the 3D tumor location from the 2D pupil

center; the ensued software simulation and error analysis; the serial communication between the tracking camera software and the simulation software; the test of the commercial available tracking camera and the stage packages; the design of the movement patterns of the stages; the system integration; the system calibration and validation experiments; and the data analysis except the implementation of the regression model to obtain the tumor center. I also participated in defining the specification for the design and revisions of the mechanical components.

References

[1] Mark F.Bear, Barry W.Connors, Michael A.Paradiso. Neuroscience: Exploring the Brain, 3rd Edition, 2006.

[2] Physiology of the ocular movements. http://telemedicine.orbis.org/data/1/rec_docs/88_Ch%204%20-%20Physiology%20of%20the%20Ocular%20Movements,%20p.%2052-84.pdf

[3] Papastefanou VP, Cohen VML. Review article: Uveal melanoma. Joural of Skin Cancer, 2011: 1-13; Doi: 10.1155/2011/573974

[4] Singh AD, Bergman L, Seregard S. Uveal melanoma: epidemiologic aspects. Ophthalmology Clinics of North America, 2005; 18: 75-84

[5] Singh AD, Tophan A. Incidence of uveal melanoma in the United States: 1973-1997. Ophthalmology, 2003; 110(5): 956-961

[6] Singh AD, Turell ME, Topham AK. Uveal melanoma: trends in incidence, treatment, and survival. Ophthalmology, 2011; 118(9): 1881-1885

[7] Singh AD, Topham A. Survival rates with uveal melanoma in the United States: 1973-1997. Ophthalmology. 2003 May; 110(5): 962-965

[8] Miller B, Abrahams C, Cole GC, Proctor NS. Ocular malignant melanoma in South African blacks. British Journal of Ophthalmology, 1981; 65(10):720-722

[9] Kuo PK, Puliafito CA, Wang KM, Liu HS, Wu BF. Uveal melanoma in China. International Ophthalmology Clinics, 1982 Fall; 22(3): 57-71

[10] Virgili G, Gatta G, Ciccolallo L, Capocaccia R, Biggeri A, Crocetti E, Lutz JM, Paci E, EUROCARE Working Group. Incidence of uveal melanoma in Europe. Ophthalmology, 2007 Dec; 114(12): 2309-2315

[11] Char DH. Ocular melanoma. Surgical Clinics of North America, 2003; 83: 253-274

[12] Albert DM. Principles and practice of ophthalmology. In: Albert, Jakobiec, editors. Philadelphia, PA: W.B.Saunders Co; 1994. Pp.3197—8, Ch.258

[13] Finger PT. Therapeutic review: Radiation therapy for chodoidal melanoma. Survey of Ophthalmology, 1997; 42(3):215-232

[14] Diener-West M, Rynolds SM, Agugliaro DJ, Caldwell R, Cumming K, Earle JD, Green DL, Hawkins BS, Hayman J, Jaiyesimi I, etc. Screening for metastasis from choroidal melanoma: the collaborative ocular melanoma study group report 23. Journal of Clinical Oncology, 2004; 22(12): 2438-2444

[15] Shields CL, Kaliki S, Furuta M, Fulco E, Alarcon C, Shields JA. American Joint Committee on Cancer Classification of posterior uveal melanoma (tumor size category) predicts Prognosis in 7731 Patients. Ophthalmology, 2013; 120(10):2066-2071

[16] Robertson DM. Changing concepts in the management of choroidal melanoma. Amerian Journal of Ophthalmology. 2003, July; 136(1):161-170

[17] McLean IW, Foster WD, Zimmerman LE. Uveal melanoma: location, size, cell type, and enucleation as risk factors in metastasis. Human Pathology. 1982, Feb.; 13(2):123-132

[18] Char DH, Miller T, Crawford J. Uveal tumor resection. British Journal of Ophthalmology. 2001; 85(10):1213-1219

[19] Malignant melanoma of the uvea. In: Edge SB, Byrd DR, Compton CC, et al., eds. : AJCC Cancer Staging Manual. 7th ed. New York, NY: Springer, 2010, pp 547-59

[20] Packard RB. Pattern of mortality in choroidal malignant melanoms. British Journal of Ophthalmology. 1980; 64 (8): 565-575

[21] Garcia-Arumi J, Sararols L, Martinez V, Corocostequi B. Vitreoretinal surgery and endoresection in high posetior choroidal melanoms. Retina. 2001; 21(5): 445-452

[22] Damato BE. Surgical resection of choroidal melanoma. In: Ryan SJ, edictor. Retina. St. Louis: C.V.Mosby, 2001: 762-772

[23] Moore RF. Choroidal sarcoma treated by intra-ocular insertion of radon seeds. British Journal of Ophthalmology. 1930; 14(4) :145-152

[24] Stallard HB. Radiotherapy for malignant melanoma of the choroid. Br J Ophthalmol. 1966; 50:147-155.

[25] Diener-West M, Earle JD, Fine SL, Hawkins BS, Moy CS, Reynolds SM, Schachat AP, Straatsma BR, Collaborative Ocular Melanoma Study Group. The COMS randomized trial of iodine 125 brachytherapy for choroidal melanoms, III: initial mortality findings. COMS Report No.18. Arch Ophthalmol. 2001 July; 119(7): 969-82

[26] Finger PT, Berson A, Ng T, Szechter A. Palladium-103 plaque radiotherapy for choroidal melanoma: an 11-year study. Int J Radioat Oncol Biol Phys. 2002 Dec. 1; 54(5): 1438-1445

[27] Lommatzsch PK. Results after beta-irradiation ($^{106}Ru/^{106}Rh$) of choroidal melanomas: 20 years' experience. Br J Ophthalmol. 1986 Nov; 70(11): 844-851

[28] Lommatzsch PK, Werschnic C, Schuster E. Long-term follow-up of Ru-106/Rh-106 brachytherapy for posterior uveal melanoms. Graefes Arch Clin Exp Ophthalmol. 2000 Feb; 238(2): 129-137

[29] Lommatzsch PK, Lommatzsch R. Treatment of juxtapapillary melanomas. Br J Ophthalmol. 1991 Dec.; 75(12): 715-717

[30] Nag S, Quivey JM, Earle JD, Followill D, Fontanesi J, Finger PT, American Brachytherapy Society. The American brachytherapy society recommendations for brachytherapy of uveal melanomas. Int J Radiation Oncology Biol Phys. 2003 Jun 1; 56(2):544-555

[31] Karvat A, Duzenli C, Ma R, Paton K, Pickles T. The treatment of choroidal melanoma with 198-Au plaque brachytherapy. Radiotherapy and Oncology. 2001 May; 59(2):153-156

[32] Finger PT. Radiation therapy for choroidal melanoma. Surv Ophthalmol. 1997 Nov-Dec.; 42(3): 215-32

[33] Finger PT. Radiation therapy for orbital tumors: concepts, current use, and ophthalmic radiation side effects. Survey of Ophthalmology. 2009 Sep-Oct.; 54(5): 545-568

[34] Hall EJ. Repair of radiation damage and the dose-rate effect. In Hall EJ (ed): Radiobiology for the Radiologist. Philadelphia, J.B. Lippincott, ed 4 1994, pp. 107-32

[35] Parsons JT, Bova FJ, Fitzgerald CR, Mendenhal WM, Million RR. Radiation retinopathy after external-beam irradiation: analysis of time-dose factors. Int J Radiat Oncol Biol Phys. 1994 Nov 15; 30(4): 765-73

[36] Finger PT. Tumour location affects the incidence of cataract and retinopathy after ophthalmic plaque radiation therapy. Br J Ophthalmol 2000 Sep; 84(9): 1068-70

[37] Astrahan MA, Luxton G, Pu Q, Petrovich Z. Conformal episcleral plaque therapy. Int J Radiation Oncoogy Biol Phys. 1997 Sep 1; 39(2):505-519

[38] Nakissa N, Rubin P, Strohl R, Keys H. Ocular and orbital complications following radiation therapy of paranasal sinus malignancies and review of literature. Cancer. 1983 Mar 15; 51(6): 980-986

[39] Wilkinson DA, Kolar M, Fleming PA, Singh AD. Dosimetric comparison of ^{106}Ru and ^{125}I plaques for treatment of shallow ($\leq$ 5mm) choroidal melanoma lesions. The British Journal of Radiology. 2008 Oct.; 81(1970): 784- 789

[40] Finger PT, Kurli M. Laser photocoagulation for radiation retinopathy after ophthalmic plaque radiation therapy. Br J Ophthalmol. 2005 Jun. ; 89(6):730-738.

[41] Roider J, Brinkmann R, Wirbelauer C, Laqua H, Bimgruber R. Subthreshold (retinal pigment epithelium) photocoagulation in macular disease: a pilot study. Br J Ophthalmol. 2000 Jan.; 84(1): 40-47

[42] Bartlema Y M, Oosterhuis JA, Joumee-de Korver JG, Tjho-Heslinga RE, Keunen JEE. Combined plaque radiotherapy and transpupillary thermotherapy in choroidal melanoma: 5 years' experience. Br J Ophthalmol. 2003 Nov.; 87(11): 1370- 1373

[43] Desjardins L, Lumbroso-Le Rouic L, Levy-Gabriel C, Dendale R, Delacroix S, Nauraye C, Esteve M, Plancher C, Asselain B. Combined proton beam radiotherapy and transpupillary thermotherapy for large uveal melanoma: a randomized study of 151 patients. Ophthalmic Research. 2006; 38(5): 255-260

[44] Shields C L, Shields JA, Perez N, Singh AD, Cater J. Primary transpupillary thermotherapy for small choroidal melanoma in 256 consecutive cases. Ophthalmology. 2002 Feb; 109(2): 225-234

[45] Pilotto E, Vujosevic S, De Belvis V, Parrozzani R, Boccassini B, Midena E. Long-term choroidal vascular changes after iodine brachytherapy versus transpupillary thermotherapy for choroidal melanoma. Eur J Ophthalmol. 2009 Jul-Aug; 19(4): 646 – 53

[46] Shildcrot Y, Wilson MW. Update on posterior uveal melanoma: treatment of eye and metastatic disease. Current Opinion in Ophthalmology. 2009 Nov; 20(6): 504- 510

[47] Krintz AL, Hanson WF, Ibbott GS, Followill DS. A reanalysis of the collaborative ocular melanoma study medium tumor trial eye plaque dosimetry. Int J Radiation Oncology Biol Phys. 2003 Jul 1; 56(3): 889 -898

[48] Seregard S, Damato B, Fleming P. Uveal malignant melanoma: management options- brachytherapy. Clinical Ophthalmic Oncology. A.Saunders. Ed. 2007: 241-247

[49] Mashayekhi A, Tuncer S, Shields CL, Shields JA. Tumour-lipid exudation after plaque radiotherapy of choroidal melanoma: the role of Bruch's membrane rupture. Ophthalmology. 2010 May; 117(5): 1013-1023

[50] Kaiserman N, Kaiseman I, Hendler K, Frenkel S, Peer J. Ruthenium-106 plaque brachytherapy for thick posterior uveal melanomas. Br J Ophthalmol. 2009 Sep.; 93(9): 1167-1171

[51] Char D H. Tumors of the eye and ocular adnexa. Toronto (BC): Decker. 2001

[52] Foss A J, Whelehan I, Hungerford JL, Anderson DF, Errington RD, Kacperek A, Restori M, Kongerud J, Sheen M. Predictive factors for the development of rubeosis following proton beam radiotherapy for uveal melanoma. Br J Ophthalmol. 1997 Sep; 81(9): 748-754

[53] Char DH, Quivey JM, Castro JR, Kroll S, Phillips T. Helium ions versus 125 I brachytherapy in the management of uveal melanoma: A prospective, randomized, dynamically balanced trial .Ophthalmology. 1993 Oct; 100(10): 1547-1554

[54] Gragoudas ES, Goitein M, Verhey L, Munzenreider J, Urie M, Suit H, Koehler A. Proton beam irradiation of uveal melanoma. Results of a 5 1/2 –year study. Arch Ophthalmol. 1982 Jun; 100(6): 928-934

[55] Fuss M, Loredo LN, Blacharski PA, Grove RI, Slater JD. Proton radiation therapy for medium and large choroidal melanoma: preservation of the eye and its functionality. Int J Radiation Oncology Biol Phys. 2001 Mar; 49(4): 1053 – 1059

[56] Munzenrider JE. Proton therapy for uveal melanomas and other eye lesions. Strahlenther Onkol. 1997; 175(Supple II) : 68 - 73

[57] Zehetmayer M. Stereotactic photon beam irradiation of uveal melanoma. Dev Ophthalmol. 2012; 49: 58 - 65

[58] Mueller AJ, Talies S, Schaller UC, Horstmann G, Wowra B, Kampik A. Stereotactic radiosurgery of large uveal melanomas with the Gamma-knife. Ophthalmology. 2000 Jul; 107(7): 1381- 1388

[59] Toktas ZO, Bicer A, Demirci G, Pazarli H, Abacioqlu U, Peker S, Kilic T.Gamma knife stereotactic radiosurgery yields good long-term outcomes for low-volume uveal melanomas without intraocular complications. Journal of Clinical Neuroscience. 2010 Apr; 17(4): 441 – 445

[60] Modorati G, Miserocchi E, Galli L, Picozzi P, Rama P. Gamma knife radiosurgery for uveal melanoma: 12 years of experience. Br J Ophthalmol. 2009 Jan; 93(1): 40-44

[61] Leksell L. The stereotactic method and radiosurgery of the brain. Acta Chir Scand. 1951 Dec 13; 102(4): 316-319

[62] Kang DW, Lee SC, Park YG, Chang JH. Long-term results of Gamma Knife surgery for uveal melanomas. J Neurosurg . 2012 Dec; 117 Suppl: 108 – 114

[63] Langmann G, Pendl G, Müllner K, Feichtinger KH, Papaefthymiouaf G. High- compared with low-dose radiosurgery for uveal melanomas. J Neurosurg. 2002 Dec; 97 (5 Supple): 640 – 643

[64] Zytkovicz A, Daftari I, Phillips TL, Chuang CF, Verhey L, Petti PL. Peripheral dose in ocular treatments with CyberKnife and Gamma Knife radiosurgery compared to proton radiotherapy. Phys Med Biol. 2007 Oct 7; 52(19): 5957 – 71

[65] Zehetmayer M, Kitz K, Menapace R, Ertl A, Heinzl H, Ruhswurm I, Georgopoulos M, Dieckmann K, Pötter R. Local tumor control and morbidity after one to three fractions of stereotactic external beam irradiation for uveal melanoma. Radiother Oncol. 2000 May; 55(2):135–44

[66] Haas A, Pinter O, Papaefthymiou G, Weger M, Berghold A, Schröttner O, Müllner K, Pendl G, Langmann G. Incidence of radiation retinopathy after high-dosage single-fraction Gamma Knife radiosurgery for choroidal melanoma. Ophthalmology. 2002 May; 109(5):909–13

[67] Pilipuf MN, Goble JC, Kassell NF. A noninvasive thermoplastic head immobilization system. J Neurosurg. 1995 June; 82(6): 1082 – 1085

[68] Bellmann C1, Fuss M, Holz FG, Debus J, Rohrschneider K, Völcker HE, Wannenmacher M. Stereotactic radiation therapy for malignant choroidal tumors: preliminary, short-term tumors. Ophthalmology. 2000 Feb; 107(2): 358 – 365

[69] Tokuuye K, Akine Y, Sumi M, Kagami Y, Ikeda H, Kaneko A. Fractionated stereotactic radiotherapy for choroidal melanoma. Radiotherapy and Oncology. 1997; 43: 87 – 91

[70] Muller K1, Naus N, Nowak PJ, Schmitz PI, de Pan C, van Santen CA, Marijnissen JP, Paridaens DA, Levendag PC, Luyten GP. Fractionated stereotactic radiotherapy for uveal melanoma, late clinical results. Radiotherapy and Oncology. 2012 Feb; 102(2): 219 – 224

[71] Georg D, Dieckmann K, Bogner J, Zehetmayer M, Pötter R. Impact of a micromultileaf collimator on stereotactic radiotherapy of uveal melanoma. Int J Radiation Oncology Biol Phys. 2003 Mar 15; 55(4): 881-891

[72] Dieckmann K, Bogner J, Georg D, Zehetmayer M, Kren G, Pötter . A linac-based stereotactic irradiation technique of uveal melanoma. Raiotherapy and Oncology. 2001 Oct; 61(1): 49-56

[73] Muller K, Nowak PJ, de Pan C, Marijnissen JP, Paridaens DA, Levendag P, Luyten GP. Effectiveness of fractionated stereotactic radiotherapy for uveal melanoma. Int J Radioat Oncol Biol Phys. 2005 Sep 1; 63(1): 116 -22

[74] Zehetmayer M1, Menapace R, Kitz K, Ertl A. Suction fixation system for stereotactic radiosurgery of intraocular malignancies. Acta Neurochir Suppl. 1995; 63: 115-118

[75] Coste-Manière E, Olender D, Kilby W, Schulz RA. Robotic whole body stereotactic radiosurgery: clinical advantages of the CyberKnife integrated system. Int J Medical Robotics and Computer Assisted Surgery. 2005 Jan; 1(2): 28-39

[76] Schweikard A, Shiomi H, Adler J. Respiration tracking in radiosurgery without fiducials. Int J Medical Robotics and Computer Assisted Surgery. 2005 Jan; 1(2): 19-27

[77] Adler JR Jr, Murphy MJ, Chang SD, Hancock SL. Image-guided robotic radiosurgery. Neurosurgery. 1999 June; 44(6): 1299-1306

[78] Choi SY, Kim MS, Yoo SY, Cho CK, Lhee CH, Lee DH, Kang JK, Shin YJ. Feasibility of image-guided robotic radiotherapy using three fractions for uveal melanoma. Tumori. 2009 Nov-Dec; 95(6): 720-725

[79] Saw CB, Chen H, Wagner H Jr. Implementation of fiducial-based image registration in the CyberKnife robotic system. Medical Dosimetry. 2008 Summer; 33(2): 156 – 160

[80] Antypas C, Pantelis E. Performance evaluation of a CyberKnife G4 image-guided robotic stereotactic radiosurgery system. Phys Med Biol. 2008 Sep 7; 53(17): 4697-4718

[81] Daftari IK, Petti PL, Larson DA, O'Brien JM, Phillips TL. A noninvasive eye fixation monitoring system for CyberKnife radiotherapy of choroidal and orbital tumors. Med Phys. 2009 Mar; 36(3): 719-724

[82] Zorlu F, Selek U, Kiratli H. Initial results of fractionated CyberKnife radiosurgery for uveal elanoma. J Neurooncol. 2009 Aug; 94(1): 111-117

[83] Mathur A, Gehrmann J, Atchison DA. Influences of luminance and accommodation stimuli on pupil size and pupil center location. Invest Opbtbalmol Vis Sci. 2014 April; 55(4):2166-2172

[84] Muller K, Nowak PJ, Luyten GP, Marijnissen JP, de Pan C, Levendag P. A modified relocatable stereotactic frame for irradiation of eye melanoma: design and evaluation of treatment accuracy. Int.J.Radiation Oncology Biol.Phys. 2004 Jan 1; 58 (1):284-291

[85] Petersch B, Bogner J, Dieckmann K, Pötter R, Georg D. Automatic real-time surveillance of eye position and gating for stereotactic radiotherapy of uveal melanoma. Med. Phys. 2004 Dec; 31(12):3521-3527

[86] Buchgeister M, Grisanti S, Süsskind D, Bamberg M, Paulsen F. A new fixation aid for the radiotherapy of eye tumors. Med Physics. 2007 Dec; 34(12): 4649-53

[87] Phillips C, Pope K, Hornby C, Chesson B, Cramb J, Bressel M. Novel 3D conformal technique for treatment of choroidal melanoma with external beam photon radiotherapy. J Med Imaging Radiat Oncol. 2013 Apr; 57(2): 230-6

[88] Erdem U, Muftuoglu O, Gundogan FC, Sobaci G, Bayer A. Pupil center shift to the coaxially sighted corneal light reflex under natural and pharmacologically dilated conditions. J Rferact Surg. 2008 May; 24(5): 530-8

[89] Tokuuye K, Akine Y, Sumi M, Kagami Y, Ikeda H, Kaneko A. Fractionated stereotactic radiotherapy for choroidal melanoma. Radiother Oncol. 1997 Apr; 43(1): 87-91

[90] Shin D, Yoo SH, Moon SH, Yoon M, Lee SB, Park SY. Eye tracking and gating system for proton therapy of orbital tumors. Med Phys. 2012 Jul; 39(7): 4265-4273

[91] McCartney AC. Pathology of ocular melanomas. Br Medical Bull, 1995 Jul; 51(3): 678-693

[92] Chen H, Wu X, Hatoum GE, Zhao W. A novel 2D/3D transformation for radiosurgery of ocular tumors: computer simulation and phantom validation. J Radiat Oncol. 2014 Sep; 3(3): 313-320

[93] Andrews DW, Bednarz G, Evans JJ, Downes B. A review of 3 current radiosurgery systems. Surgical Neurology. 2006 Dec; 66(6): 559 – 564

[94] Bianciotto C, Shields CL, Lally SE, Freire J, Shields JA. CyberKnife radiosurgery for the treatment of intraocular and periocular lymphoma. Arch Ophthalmol. 2010 Dec; 128(12):1561-1567

[95] H Chen, X Wu, G F Hatoum, A Gonzalez, R Garcia, W Zhao, A mechanical eyeball phantom for uveal melanoma radiosurgery by cyberknife, J Radiat Oncol, 2014; DOI: 10.1007/s13566-014-0165-4